AD-A124 067 FORCE AND PRESSURE MEASUREMENTS ON A RESEARCH MODEL WITH A LOW- MID- AND.. (U) GENERAL DYNAMICS FORT WORTH TX FORT WORTH DIV R A COX DEC 82 FZA-540-VOL-1 1/1

UNCLASSIFIED N00014-82-C-0340 F/G 1/3 NL

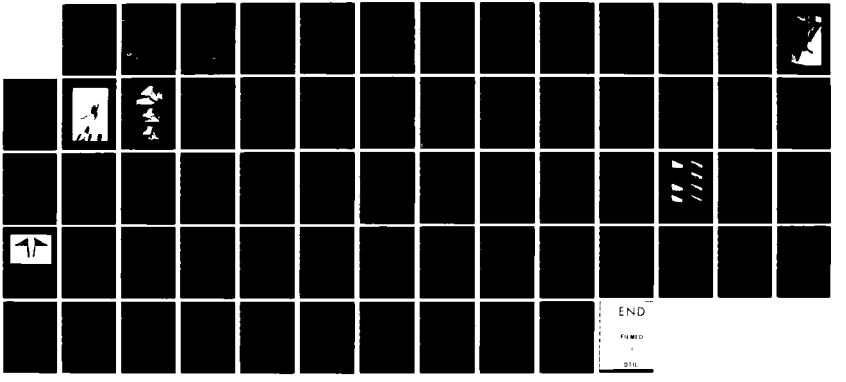

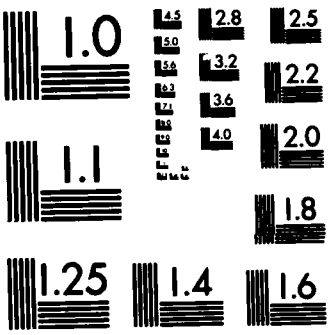

COPY

AD A 124067

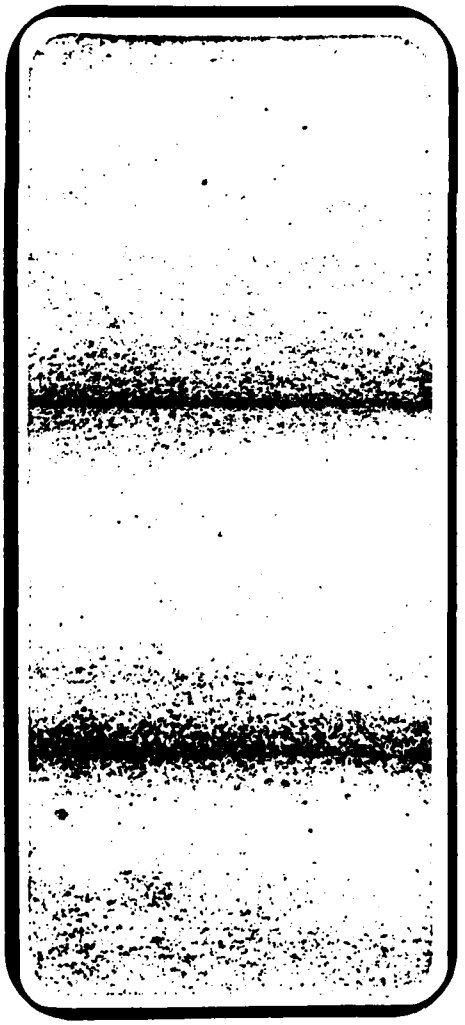

FORCE AND PRESSURE MEASUREMENTS ON A RESEARCH MODEL WITH A LOW-, MID-, AND T-TAIL AT MACH NUMBERS OF 0.60 TO 0.90

VOLUME I - SUMMARY REPORT

R. A. Cox

GENERAL DYNAMICS
Fort Worth Division

(12)

Contract N00014-82-C-0340

December 1982

FINAL REPORT

Prepared For The
OFFICE OF NAVAL RESEARCH

Unclassified

SECURITY CLASSIFICATION OF THIS PAGE (When Data Entered)

REPORT DOCUMENTATION PAGE		READ INSTRUCTIONS BEFORE COMPLETING FORM
1. REPORT NUMBER General Dynamics Report No. FZA-540	2. GOVT ACCESSION NO. AD-A124 067	3. RECIPIENT'S CATALOG NUMBER
4. TITLE (and Subtitle) Force and Pressure Measurements on a Research Model with a Low-,Mid-, and T-Tail at Mach Numbers of 0.60 to 0.90; Volume I - Summary Report		5. TYPE OF REPORT & PERIOD COVERED Final Report 15 April 1982 - 14 Dec 1982 6. PERFORMING ORG. REPORT NUMBER N/A
7. AUTHOR(s) Cox, Ronald A.		8. CONTRACT OR GRANT NUMBER(s) N00014-82-C-0340
9. PERFORMING ORGANIZATION NAME AND ADDRESS General Dynamics, Fort Worth Division P. O. Box 748 Fort Worth, Texas 76101		10. PROGRAM ELEMENT, PROJECT, TASK AREA & WORK UNIT NUMBERS P.E. 62241N RF 41-411-801 NR 212-274
11. CONTROLLING OFFICE NAME AND ADDRESS Office of Naval Research 800 N. Quincy Street Arlington, Virginia 22217		12. REPORT DATE December 1982 13. NUMBER OF PAGES
14. MONITORING AGENCY NAME & ADDRESS(if different from Controlling Office)		15. SECURITY CLASS. (of this report) Unclassified 15a. DECLASSIFICATION DOWNGRADING SCHEDULE

16. DISTRIBUTION STATEMENT (of this Report)

Approved for public release, distribution unlimited.

17. DISTRIBUTION STATEMENT (of the abstract entered in Block 20, if different from Report)

18. SUPPLEMENTARY NOTES

19. KEY WORDS (Continue on reverse side if necessary and identify by block number)

20. ABSTRACT (Continue on reverse side if necessary and identify by block number)

An investigation of the effects of a low-, mid-, and T-tail on configuration aerodynamics was carried out in the NASA/Ames Research Center 14-Foot Transonic Wind Tunnel. A baseline wing and a wing refined with the use of numerical optimization were tested alone and in conjunction with a horizontal tail in a low-, mid-, and T-Tail arrangement. Wing and horizontal tail pressure data and force data were obtained in the Mach number range 0.60 to 0.90 and at angles of attack from -6 to +28 deg. The all-flying horizontal tail was tested at deflection angles of -10,0, and +10 deg. The refined wing showed positive drag improvements over most of the Mach number range. The low-tail proved to be slightly more favorable than the T-Tail at low C_L's.

DD FORM 1 JAN 73 1473 EDITION OF 1 NOV 65 IS OBSOLETE

Unclassified

SECURITY CLASSIFICATION OF THIS PAGE (When Data Entered)

SUMMARY

An investigation of the effects of a low-, mid-, and T-tail on configuration aerodynamics was carried out in the NASA/Ames Research Center 14-Foot Transonic Wind Tunnel. A baseline wing and a wing refined with the use of numerical optimization were tested alone and in conjunction with a horizontal tail in a low-, mid-, and T-tail arrangement. The refined wing airfoil sections were obtained by perturbing from the baseline wing sections in order to satisfy specified design criteria. Chordwise pressure distributions utilized in the numerical optimization were computed with the Bailey-Ballhaus transonic, small-disturbance code.

Wing and horizontal tail pressure data and force data were obtained in the Mach number range 0.60 to 0.90 and at angles of attack from -6 to +28 deg. The all-flying horizontal tail was tested at deflection angles of -10, 0, and +10 deg.

The refined wing showed positive drag improvements over most of the Mach number range. A larger trim drag was associated with the refined wing because of a decrease in the configuration C_{mo}.

The low-tail proved to be slightly more favorable than the T-tail at low C_L's. Apparent body-induced downwash complicated the analysis of the mid-tail.

PREFACE

The wind tunnel test outlined in this report was sponsored by the Office of Naval Research , the NASA/Ames Research Center, and the Naval Air Systems Command under Contract No. N00014-82-C-0340 and executed by General Dynamics Corporation. The contracted activity spans the period from 15 April 1982 through 14 December 1982. Tests were conducted in June and July of 1982 at the NASA/Ames Research Center 14-Foot Transonic Wind Tunnel. The research model, designated 603E, was manufactured in part under ONR Contract No. N00014-81-C-0680.

The program activities were monitored by Dr. Robert E. Whitehead of ONR. Additional support was provided by Ray M. Hicks of NASA/Ames Research Center. The program was managed by Ronald A. Cox of the Fort Worth Division and the tests were conducted by R. J. Cochi.

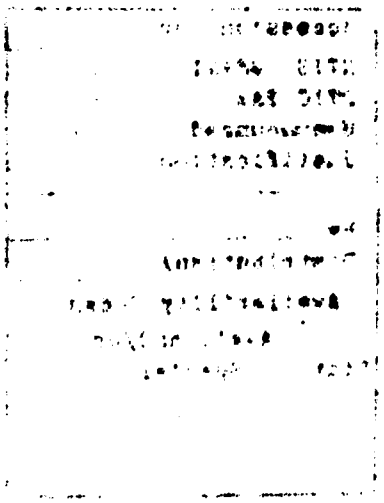

TABLE OF CONTENTS

LIST OF ILLUSTRATIONS

LIST OF ILLUSTRATIONS (Cont'd)

LIST OF ILLUSTRATIONS (Cont'd)

LIST OF TABLES

1 INTRODUCTION

Model 603E, shown in Figure 1, is used to research subsonic and transonic configuration aerodynamics. The model is of a trainer-type configuration with a two-man cockpit and side mounted flow-through nacelles. The model's baseline wing can be tested with the leading- and trailing-edge flaps deflected. The horizontal stabilizer can be located in a low-, mid-, or T-tail arrangement and used as an all-flying tail or with a deflected elevator.

The present study was undertaken to provide wind tunnel force and pressure data on the model configured with one of two wings designed for transonic flight and with the horizontal tail in any one of three vertical positions. The data can then be used to evaluate the performance of the two research wings and for determining the influence of horizontal tail location on tail aerodynamics when it is in the downwash field of a wing-body combination.

Volume II of this report contains a description of the model tested and a tabulation of the data obtained. This volume presents an analysis and summary of the data obtained during the subject test.

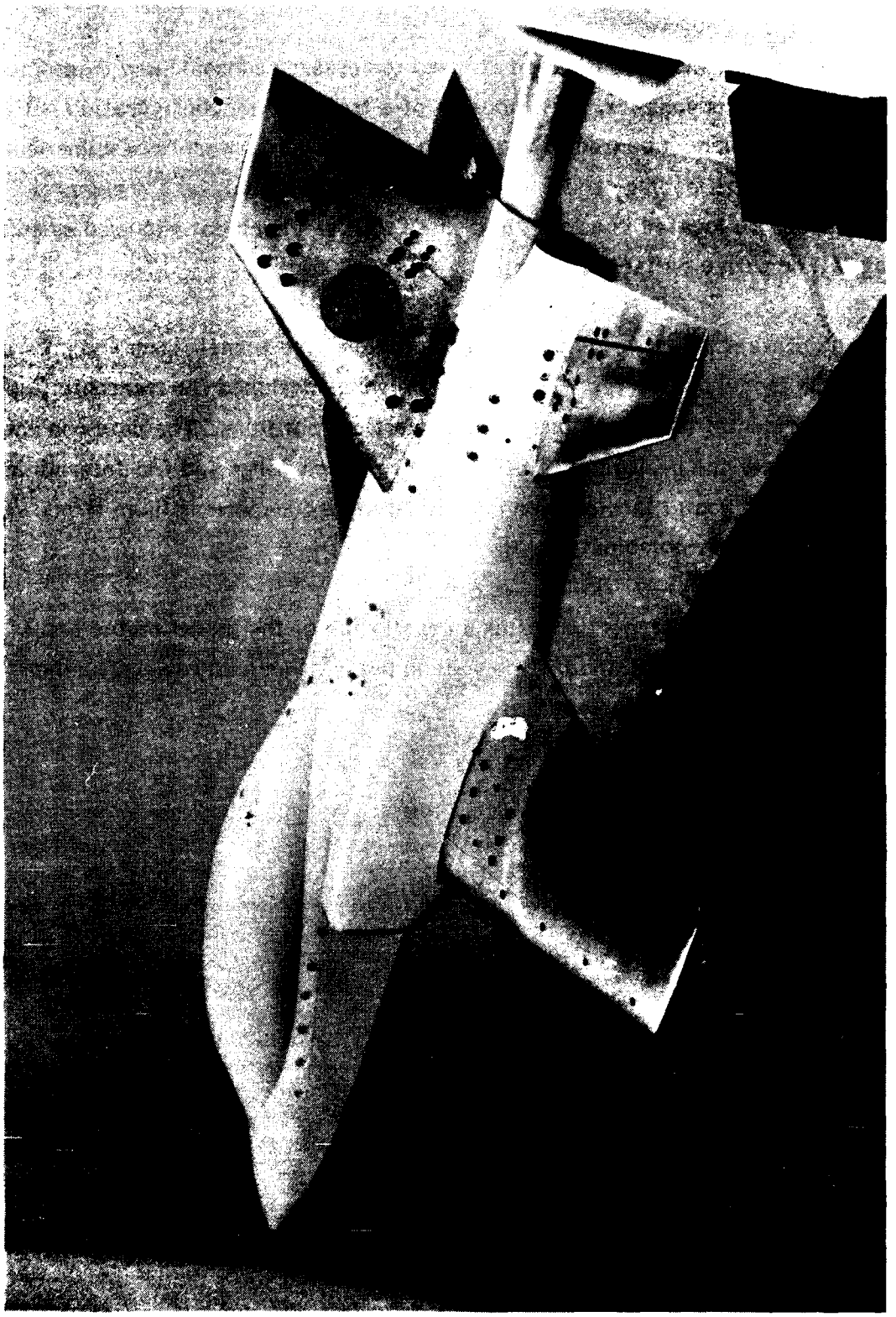

Figure 1. Three-quarter rear view of model 603E.

2 TEST AND MODEL DESCRIPTION

Model 603E is shown installed in the NASA/ARC 14-Foot Transonic Wind Tunnel in Figure 2. The model is of a trainer-type configuration and is used as an aerodynamic research model. The steel, aluminum, and fiberglass model can be equipped with an all flying low-, mid-, or T-tail at deflections of -10, 0, or +10 deg. Figure 3 shows the tail installed in the three positions.

A baseline (steel) wing and an alternate (aluminum) wing are interchangeable on the model. The baseline wing, designated W9, incorporates a NASA supercritical airfoil along linear element lines. The alternate wing, W10, is of identical planform but with chordwise airfoil sections optimized for transonic cruise. Wing W10 airfoil sections were obtained by using an optimization routine to perturb from the Wing W9 sections in order to satisfy specified design criteria. Chordwise pressure distributions utilized in the numerical optimization were computed with the Bailey-Ballhaus transonic, small-disturbance code. The approach used in the design of wing W10 is discussed in Reference 1. A description of the Bailey-Ballhaus code can be found in Reference 2.

The wing and vertical tail planform geometries are shown in Figure 4, the horizontal tail in Figure 5. The configurations' primary dimensions are listed in Table 2.1. Fuselage cross-sections are shown in Figure 6.

Model 603E is instrumented with 55 surface static pressures located in the wing and horizontal tail. Both the baseline and the alternate wing pressures are located at a non-dimensionalized span station of η =0.545. The horizontal tail pressures are located at an exposed span station of η=0.628.

The subject investigations were carried out in the NASA/ARC 14-Foot Transonic Wind Tunnel during the period 21 June 1982 through 2 July 1982. The test was designated ARC 441-14 and consisted of 92 runs, requiring 192.5 hours of occupancy time. The tests were conducted at Mach numbers varying from 0.60 to 0.90 which resulted in Reynolds numbers that ranged from approximately 11. to 13. x 10^6 per meter, respectively (3.3 to 3.9 x 10^6 per foot). The configuration angle of attack (referenced to the body waterline) was varied from -6 to +28 deg and the

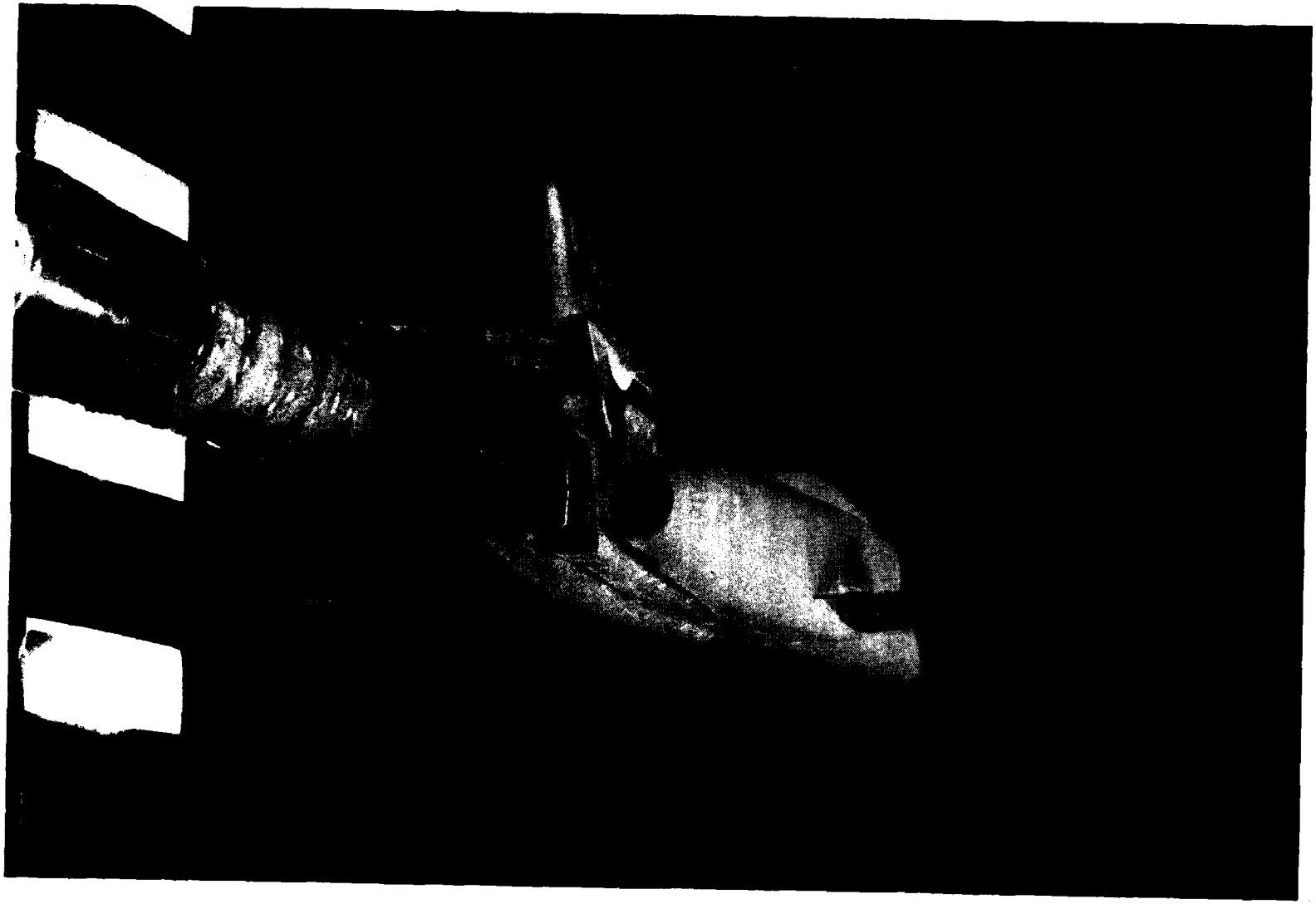

Figure 2. Model 603E installed in the NASA/ARC 14-Foot Wind Tunnel.

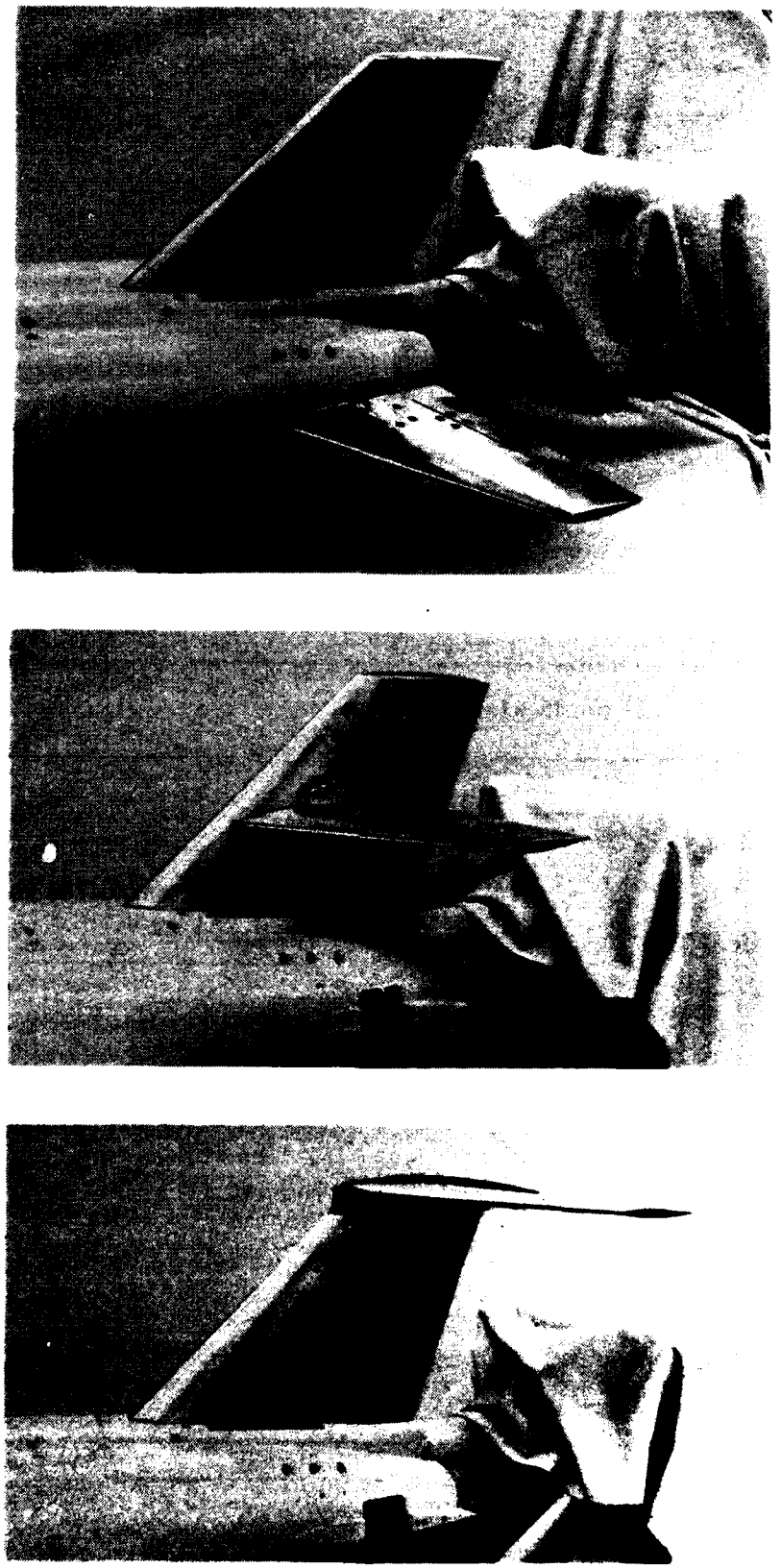

Figure 3. Low-, mid-, and T-Tail positions.

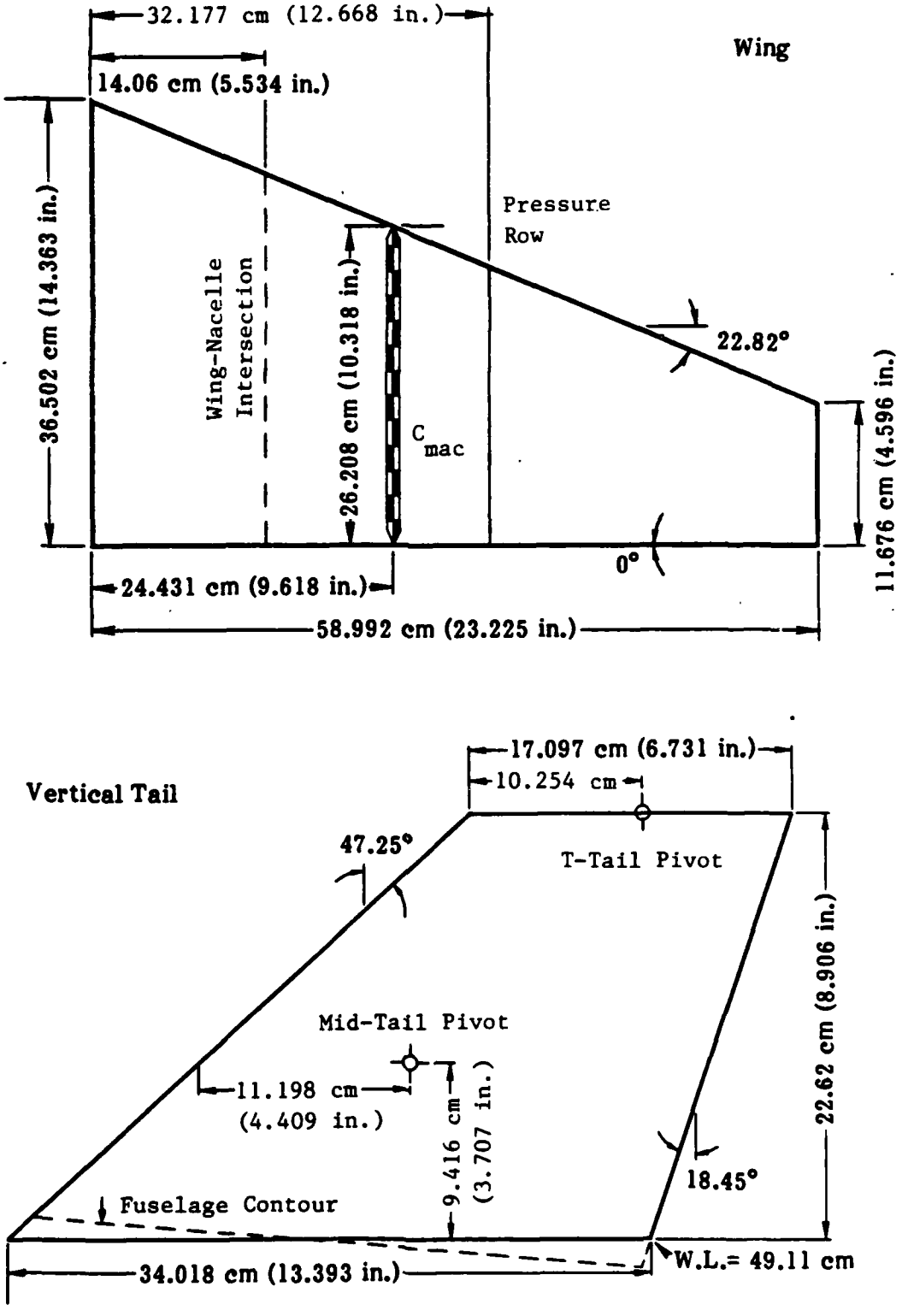

Figure 4. Wing and vertical tail planform geometries.

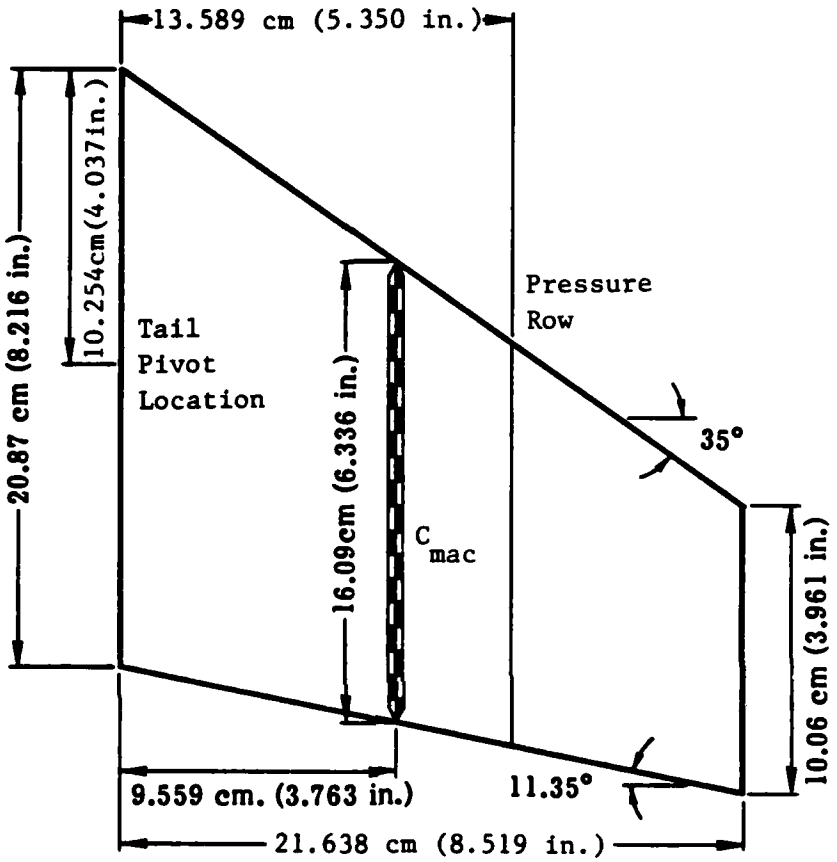

Horizontal	Apex Location		
	F.S.	S.S	W.L.
H_7 (T)	141.24 cm (55.606 in.)	1.354 cm (.533 in.)	71.727 cm (28.239 in.)
H_{7a} (Mid)	128.99 cm (50.782 in.)	1.349 cm (.531 in.)	58.522 cm (23.040 in.)
H_{7b} (Low)	128.99 cm (50.782 in.)	14.046 cm (5.530 in.)	41.554 cm (16.360 in.)

Figure 5. Horizontal tail geometry and locations.

TABLE 2.1 GENERAL GEOMETRIC CHARACTERISTICS

Reference Wing Planform Geometry (W_9)	
Wing area	0.2842 m^2 (440.53 $in.^2$)
Wing apex location	
Fuselage station	74.922 cm (29.497 in.)
Span station	0.0 cm (0.0 in.)
Waterline	36.848 cm (14.507 in.)
Aspect ratio	4.900
Wing half span	58.992 cm (23.225 in.)
Leading-edge sweep	22.82°
Trailing-edge sweep	0°
Taper ratio	0.3200
Root chord (• ℄)	36.502 cm (14.363 in.)
Tip chord	11.676 cm (4.596 in.)
Mean aerodynamic chord	26.208 cm (10.318 in.)
Leading-edge location (fuselage station)	85.202 cm (33.544 in.)
Lateral location (span station)	24.431 cm (9.618 in.)
Moment reference (0.30 C_{MAC})	
Fuselage station	93.053 cm (36.635 in.)
Span station	0.00 cm (0.00 in.)
Waterline	40.64 cm (16.000 in.)
Airfoil section	
Root	SC(2)-0414
Tip	SC(2)-0410
Twist (trailing-edge up, 0° • ℄)	-3°
Dihedral (tip up)	1°
Incidence (trailing-edge down)	2°
Vertical Tail (V_3) (exposed)	
Area	578.1 cm^2 (89.61 $in.^2$)
Apex location	
Fuselage station	117.9 cm (46.4 in.)
Span station	0.0 cm (0.0 in.)
Waterline	49.11 cm (19.333 in.)
Aspect ratio	1.770
Half Span	22.62 cm (8.906 in.)
Leading-edge sweep	47.25°
Trailing-edge sweep	18.45°
Taper ratio	0.5026
Root chord (W.L.= 49.11 cm)	34.018 cm (13.393 in.)
Tip chord	17.097 cm (6.731 in.)
Mean aerodynamic chord	26.491 cm (10.430 in.)
Leading-edge location (fuselage station)	128.74 cm (50.686 in.)
Waterline location	59.168 cm (23.295 in.)
Airfoil section	Upper surface of airfoil SC(2)-0410 (symmetric)

TABLE 2.1 GENERAL GEOMETRIC CHARACTERISTICS

(Continued)

Horizontal Tail Actuator Fairing (X_7) (for use with H_7)	
Forward extent (fuselage station)	140.29 cm (55.233 in.)
Rearward extent (fuselage station)	166.62 cm (65.6 in.)
Waterline location	71.727 cm (28.239 in.)
Horizontal Tail (H_7, H_{7a}, H_{7b},)	
Area	669.3 cm^2 (103.74 $in.^2$)
Aspect ratio	2.798
Half span	21.638 cm (8.519 in.)
Leading-edge sweep	35°
Trailing-edge sweep	11.35°
Taper ratio	0.4821
Root chord	20.87 cm (8.216 in.)
Tip chord	10.06 cm (3.961 in.)
Mean aerodynamic chord	16.09cm (6.336 in.)
Leading-edge location (from apex)	6.693 cm (2.635 in.)
Lateral location (from apex)	9.559 cm. (3.763 in.)
Airfoil section	64A010
Body (B_{3M})	
Length (nose to nacelle aft end)	136.00 cm (53.544 in.)
Nose location (fuselage station)	13.546 cm (5.333 in.)
Nacelle (N_6)	
Average lateral wing-body intersection (span station)	14.06 cm (5.534 in.)
Forward extent (fuselage station) nacelle face canted forward 5° about W.L. = 42.164 cm (16.600 in.)	73.558 cm (28.960 in.)
Rearward extent (fuselage station) nacelle exit is canted in 2° and down 2° about WL = 41.554 cm (16.360 in.)	149.55 cm (58.877 in.)
Inlet throat area (FS = 76.2 cm)	50.46 cm^2 (7.822 in^2)
Exit throat area (FS = 149.55 cm)	42.32 cm^2 (6.56 $in.^2$)

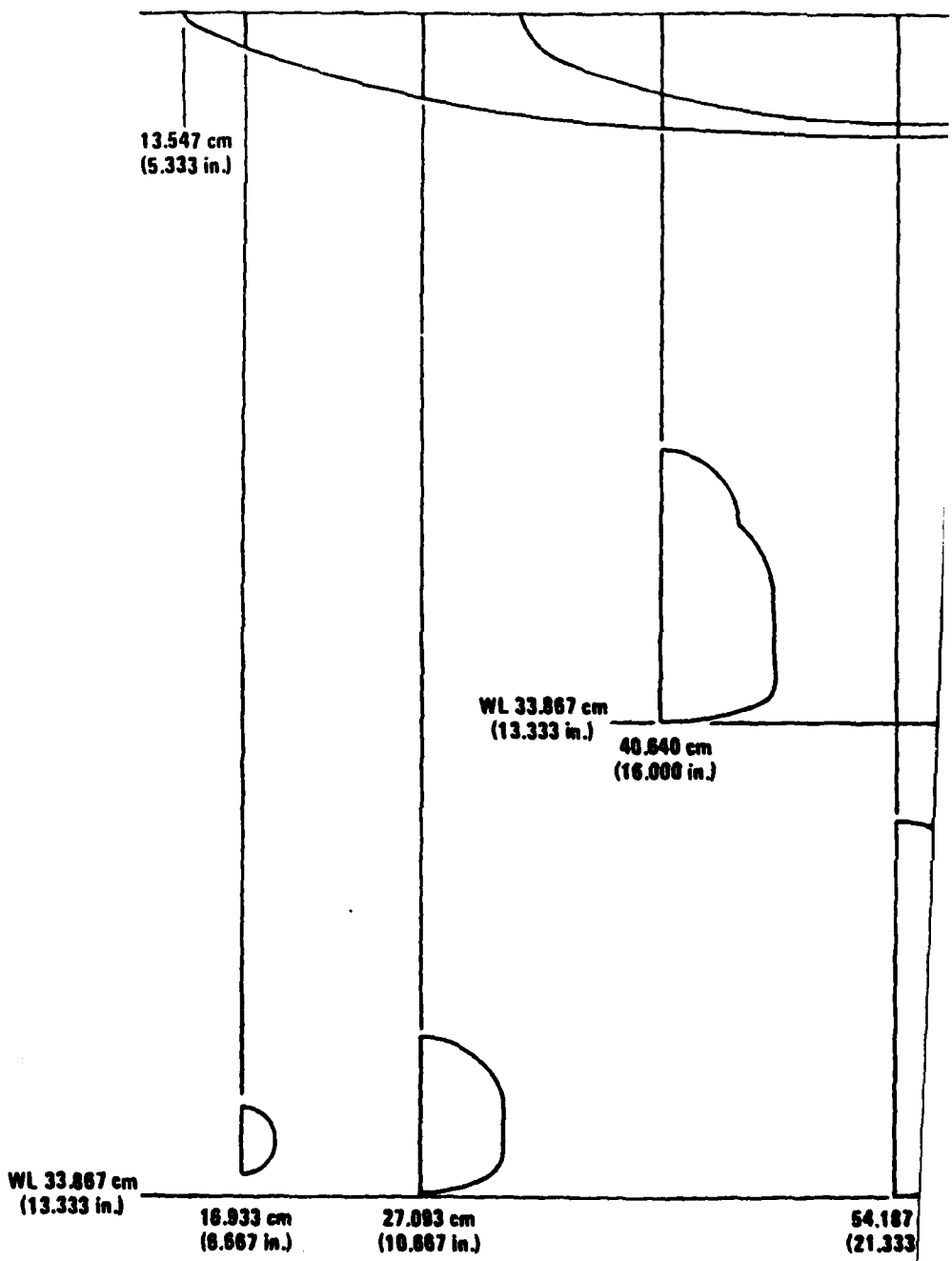
13.547 cm
(5.333 in.)
WL 33.867 cm
(13.333 in.)
40.640 cm
(16.000 in.)
WL 33.867 cm
(13.333 in.)
16.933 cm
(6.667 in.)
27.093 cm
(10.667 in.)
54.187
(21.333

nch = 4 Model Inches

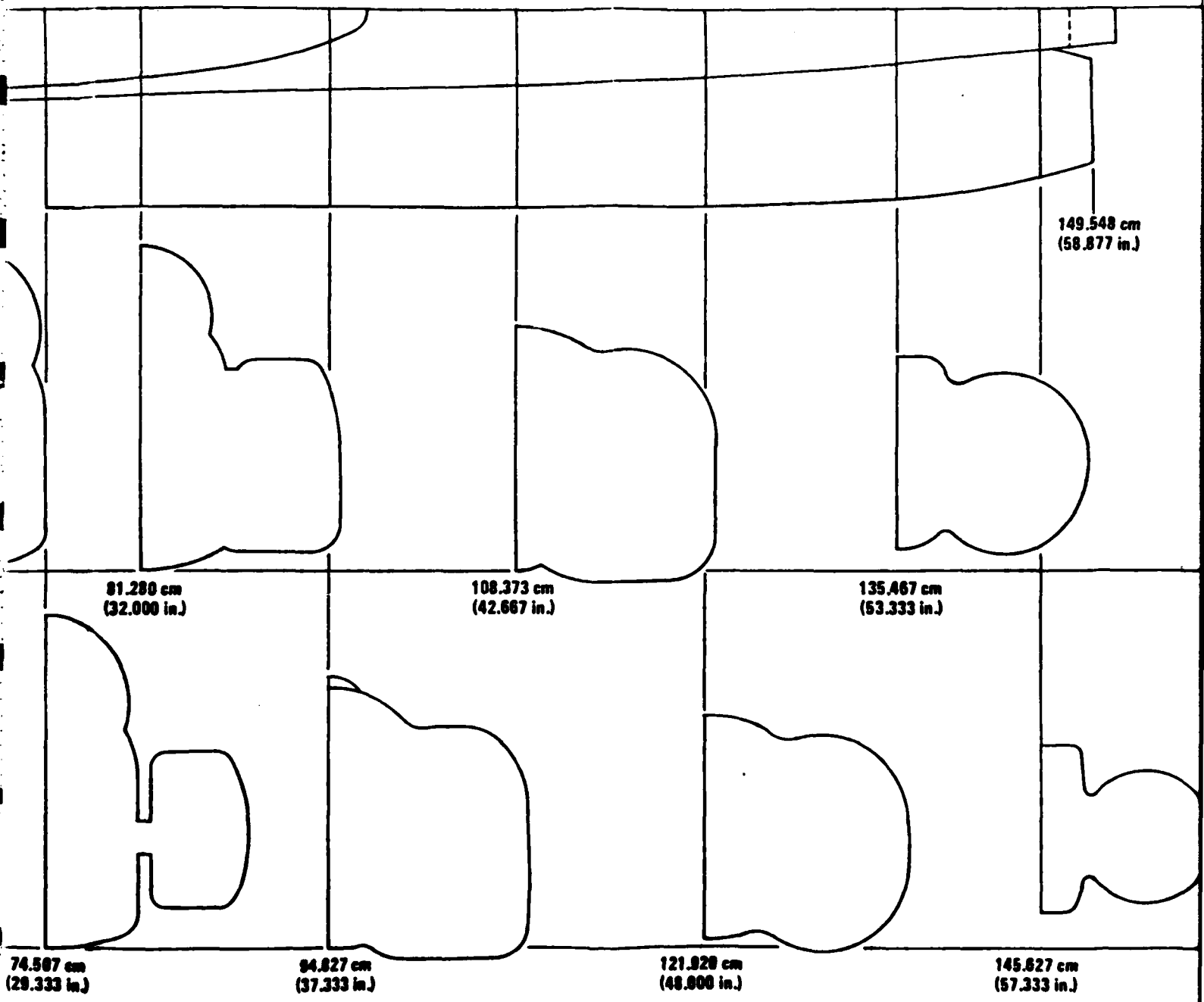

Figure 6. Fuselage cross-sections.

horizontal tail was tested at -10, 0, and +10 deg. The wing is at an incidence of +2 deg to the body.

The model geometry, test Mach numbers, and pitch schedules run during test ARC 441-14 are listed in the test run schedule presented in Table 2.2. Force, pressure and oil flow visualization data were obtained.

Table 2.2 NASA/ARC Test 441-14 Run Schedule

CONFIGURATION						MACH / RUN NUMBER								REMARKS
COMPONENTS	NO.	α SCH	β deg	ϕ deg	δ_H deg	0.60	0.70	0.75	0.78	0.80	0.82	0.85	0.90	
B N V R W H 3m 6 3 2 9 7b	1	A	0	0	0	1			2			3		PRESSURE PHASE
	1	B			-10	4			5			6		
	1	C			+10	7			8			9		
B N V R W 3m 6 3 2 9	2	D			OFF	10	11	12	13	14	15	16	17	
B N V R W H 3m 6 3 2 9 7a	3	A			0	18			19			20		
	3	A			-10	21			22			23		
B N V R W H 3m 6 3 2 9 7	4	E			0	24			25			26		
B N V R W H 3m 6 3 2 10 7	5	E			0	27			28			29		
B N V R W 3m 6 3 2 10	6	D			OFF	30	31	37	32	33	34	35	36	
B N V R W H 3m 6 3 2 10 7b	7	A			0	38			39			40		
	7	A			-10	41			42			43		
	7	A			-10	44			45			46		FORCE PHASE
	7	A			0	47			48			49		
B N V R W H 3m 6 3 2 10 7	5	E			0	50			51			52		
B N V R W 3m 6 3 2 10	6	D			OFF	53	54	55	56	57	58	59	60	
	6	F			OFF				61					**
	6	C			OFF				62					**
B N V R W 3m 6 3 2 9	2	D			OFF	63	64	65	66	67	68	69	70	
	2	H			OFF				71					**
B N V R W H 3m 6 3 2 9 7b	1	A			0	72			73			74		
	1	A			-10	75			76			77		
	1	C			+10	78			79			80		
B N V R W H 3m 6 3 2 9 7	4	E			0	81			82			83		
	4	A			-10	84			85			86		
B N V R W H 3m 6 3 2 9 7a	3	A			0	87			88			89		
	3	A			-10	90			91			92		

** = Oil Flow

α SCHEDULES (degrees)

A -6 to +20 ($\Delta\alpha$ = 2)
B -6 to +26 ($\Delta\alpha$ = 2)
C -6 to +10 ($\Delta\alpha$ = 2)
D -6 to +8 ($\Delta\alpha$ = 1), +10 to +18 ($\Delta\alpha$ = 2)
E -6 to +16 ($\Delta\alpha$ = 2), +17
F +2, +3, +4
G +2, +3, +6
H +2, +3, +6

3 TEST RESULTS

The force and static pressure data obtained during test ARC 441-14 are tabulated in its entirety in Volume II of this report. The following discussions encompass a portion of those data.

3.1 MACH NUMBER EFFECTS

Drag-rise curves of model 603E (tail off and low-tail trim increments) at C_L=0.5 are displayed in Figure 7. A noticeable break in the drag versus Mach number curve occurs at about M_∞=0.78. For the tail-off configurations, a major reduction in drag creep is achieved with wing W10; however, higher trim drag associated with W10 negates some of the gains.

Wing W9 pressure data are presented in Figure 8 for α=2.9 deg and M_∞=0.75, 0.78, 0.80, 0.82, 0.85, and 0.90. The open and filled data symbols depict the upper surface and the lower surface pressures respectively throughout the entire report. The rapid increase in drag at Mach numbers greater than M_∞=0.78 can be traced to several well known separation-forced modifications to transonic pressure distributions. The first principal change, that can be attributed to separation, is the arrest in the aft shock motion that occurs between M_∞=0.78 and M_∞=0.80. The shock starts a forward motion between M_∞=0.80 and 0.85 and reverses again, moving aft, as seen at M_∞=0.90. This type of behavior is discussed in full in Reference 3.

The start of the forward shock motion, between M_∞=0.80 and 0.82, concurs with a divergence in trailing-edge pressure (as observed in Figure 8, assuming a linear extrapolation of C_p from x/c=0.95 to the trailing edge). As Mach number is increased, the trailing-edge pressure continues to decrease.

As the freestream Mach number is increased from 0.85 to 0.90, a third feature of transonic flow that contributes to drag rise is observed on the lower surface. At Mach numbers below about 0.85, the flow begins to recompress near mid-chord due to the cusp. At M_∞=0.85 a local region of separation apears to occur at about 80 percent of chord. In contrast to the mid-chord recompression at lower Mach numbers, at M_∞=0.90 a rapid expansion is observed followed by a (shock)

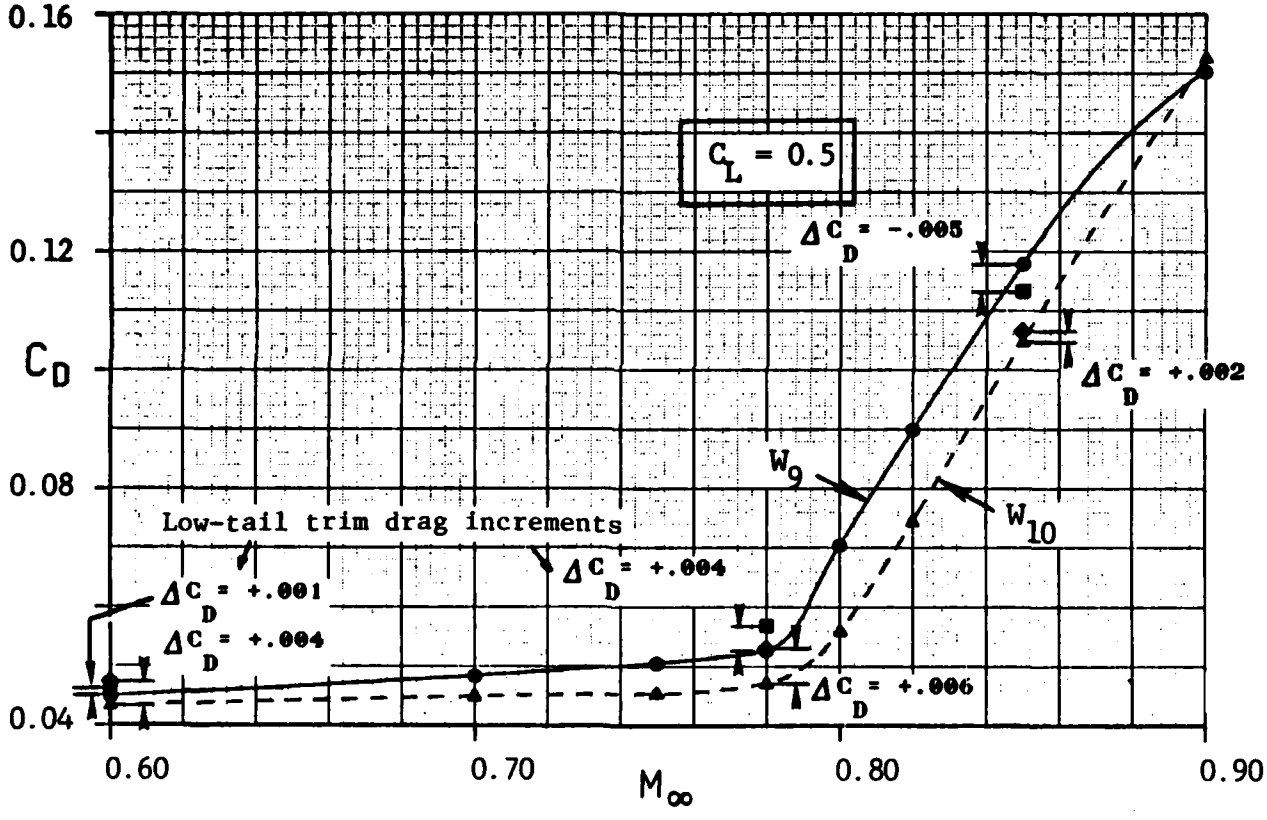

Figure 7 Configuration drag-rise.

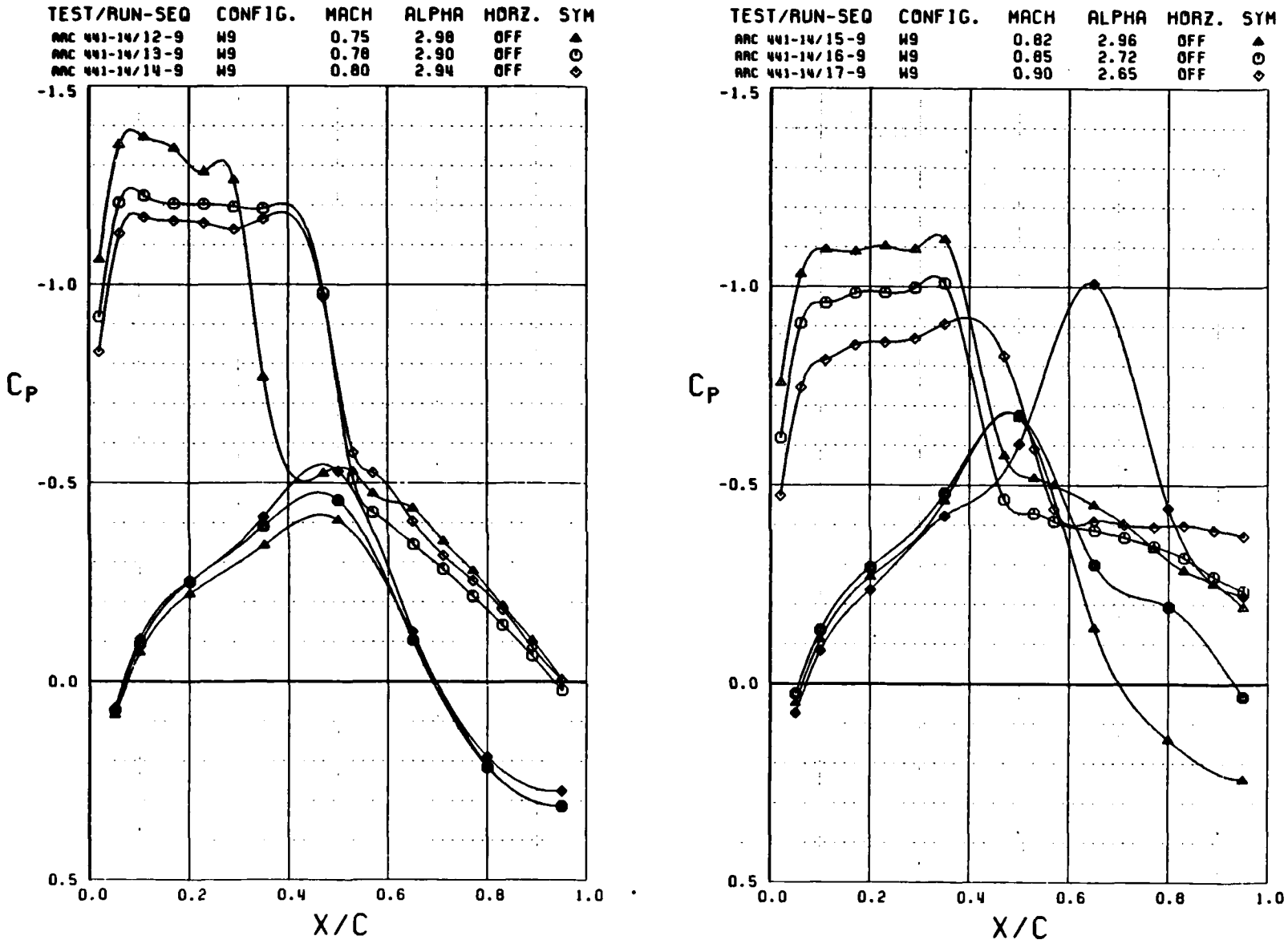

Figure 8 Effect of Mach number on wing pressures.

recompression to a negative trailing-edge pressure. The formation of this lower-surface shock can be attributed both to high (negative) pressures near mid-chord and to forced flow acceleration caused by the negative pressures at the trailing edge on the upper surface.

The reduction in suction at the leading edge, with increasing Mach number, also contributes to the drag rise; however, this behavior is not always observed.

As Mach number is increased the configurations lift curve slope initially increases to a maximum value at about M_∞=0.82, followed by a rapid decrease at M_∞=0.85. See Figure 9.

The angle of attack at which trailing-edge separation first occurs on the upper surface (as defined by a negative trailing-edge pressure) at span station 32.177 cm (12.668 in.) is displayed as a function of Mach number in Figure 10 for wings W9 and W10 with the tail off. The data trend shows a distinct decrease in separation threshold above M_∞=0.70. Data at this one span station, however, do not necessarily represent the flow behavior on the rest of the wing. An analysis of C_L-α data showed a break in the lift curve slope at an angle of attack of 0 to 1 deg below the angle of attack for pressure divergence.

3.2 WING/BODY CHARACTERISTICS

A brief analysis of tail-on and tail-off data did not reveal any significant change in wing pressures due to the addition of the horizontal tail or its placement at moderate angles of attack. The following discussions deal mainly with the wing alone cases.

3.2.1 Wings W9 and W10 Force Data

The modifications to the W9 airfoil sections to arrive at wing W10 consisted primarily of a leading-edge droop and an aft displacement of camber. These modifications tended to decrease shock strength at the expense of an increase in nose-down pitching moment.

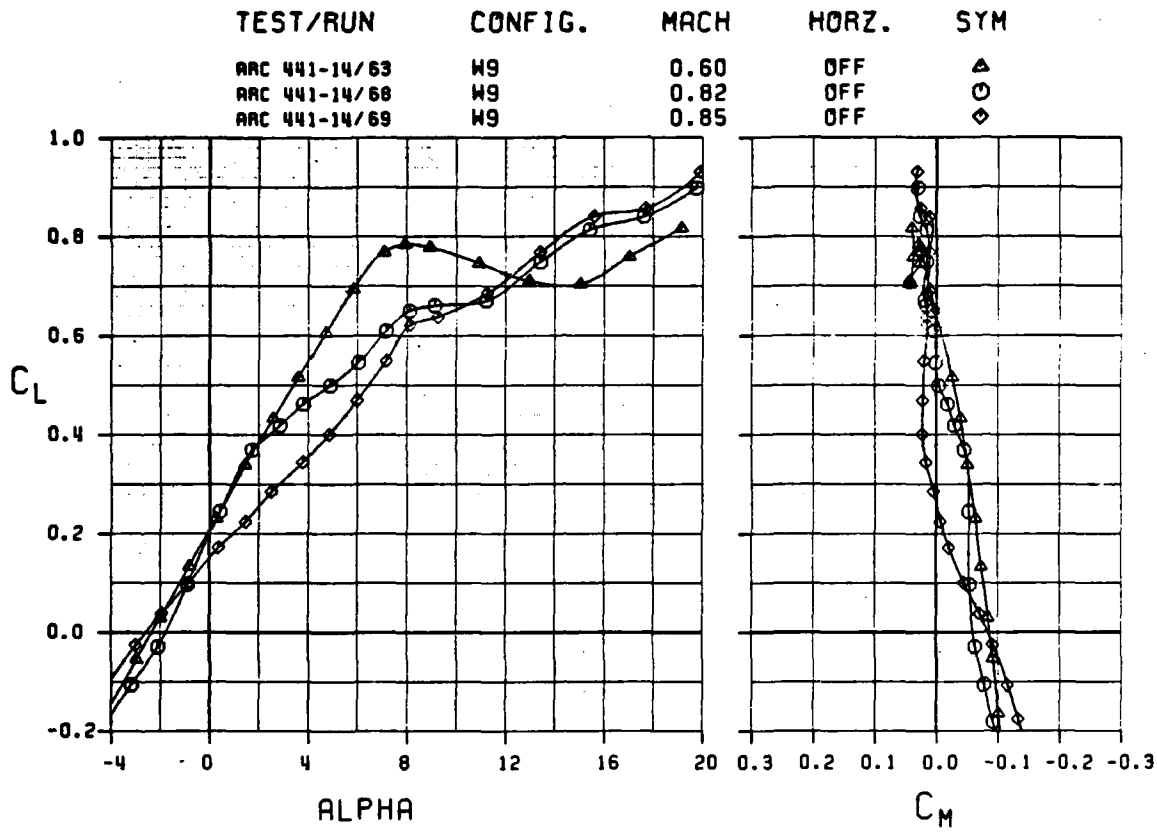

Figure 9 Change in lift curve with Mach number.

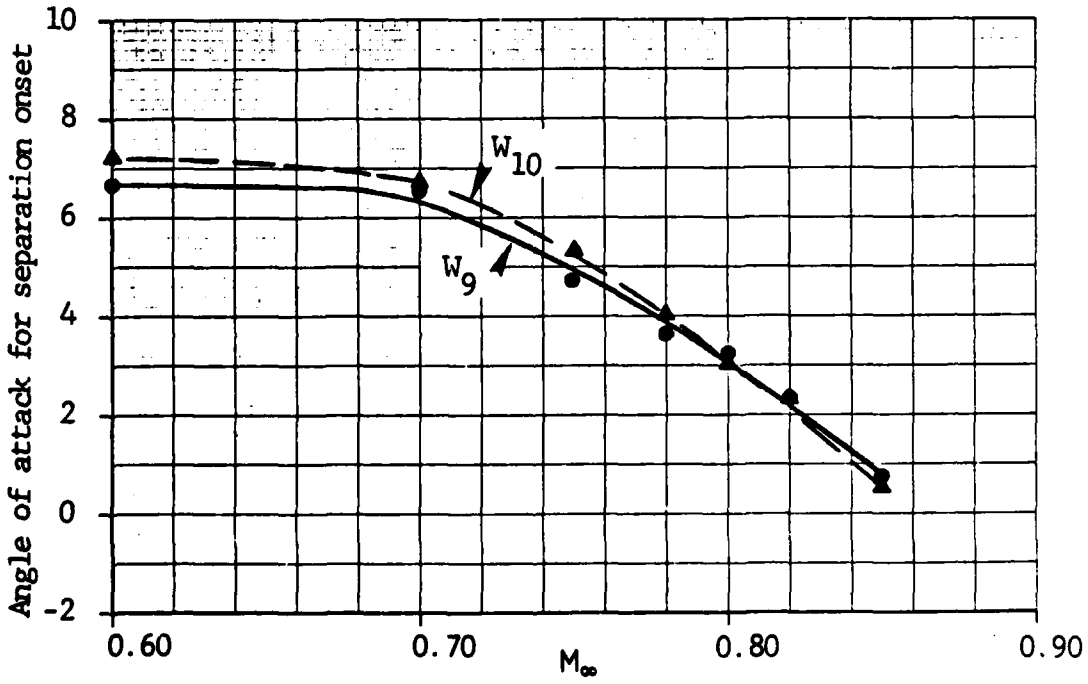

Figure 10 Trailing-edge separation occurrence at η=0.545.

Figures 11 through 14 present the lift curves and pitching moment data for wings W9 and W10 at Mach numbers of 0.60, 0.78, 0.80, and 0.85, respectively. The lift curve slopes of both wings are approximately the same except at M_∞=0.85. An analysis of the wing pressures at M_∞=0.85 revealed slightly more negative pressures in the cusp of W9 than W10, though probably not enough to cause the difference. Flow degradation at the root is suspected. Wing W10 attains a somewhat higher $C_{L_{max}}$ across the entire Mach number range, due most likely to the leading-edge droop.

The negative moment shift of wing W10 from wing W9 remains fairly constant at and below M_∞=0.82, which implies a stationary center of pressure. There is a slight (positive) break in the moment curve at the C_L corresponding to the break in the configurations C_L-α curve.

The drag data corresponding to Figures 11 through 14 are presented in Figures 15 through 18. The M_∞=0.60 data vary smoothly for both wings. At higher Mach numbers drag rise takes place initially for wing W9 followed at a slightly higher C_L for wing W10. The break in drag begins at C_L=0.5 for M_∞=0.78 and occurs at progressively lower C_L's as Mach numbers is increased. The break in the drag polar corresponds well with the C_L-α break.

The trimmed drag polars for wings W9 and W10 in the low-tail configuration are presented in Figures 19, 20, and 21 for Mach numbers of 0.60, 0.78, and 0.85, respectively. The drag increments between the two wings are reduced over that of the wing-alone case. The trim-drag decrement for wing W10 could probably be reduced by a shift in the wing location on the model. A detailed design would be needed to make these type of allowances. One other area of improvement for W10 is at low C_L's for M_∞=0.85.

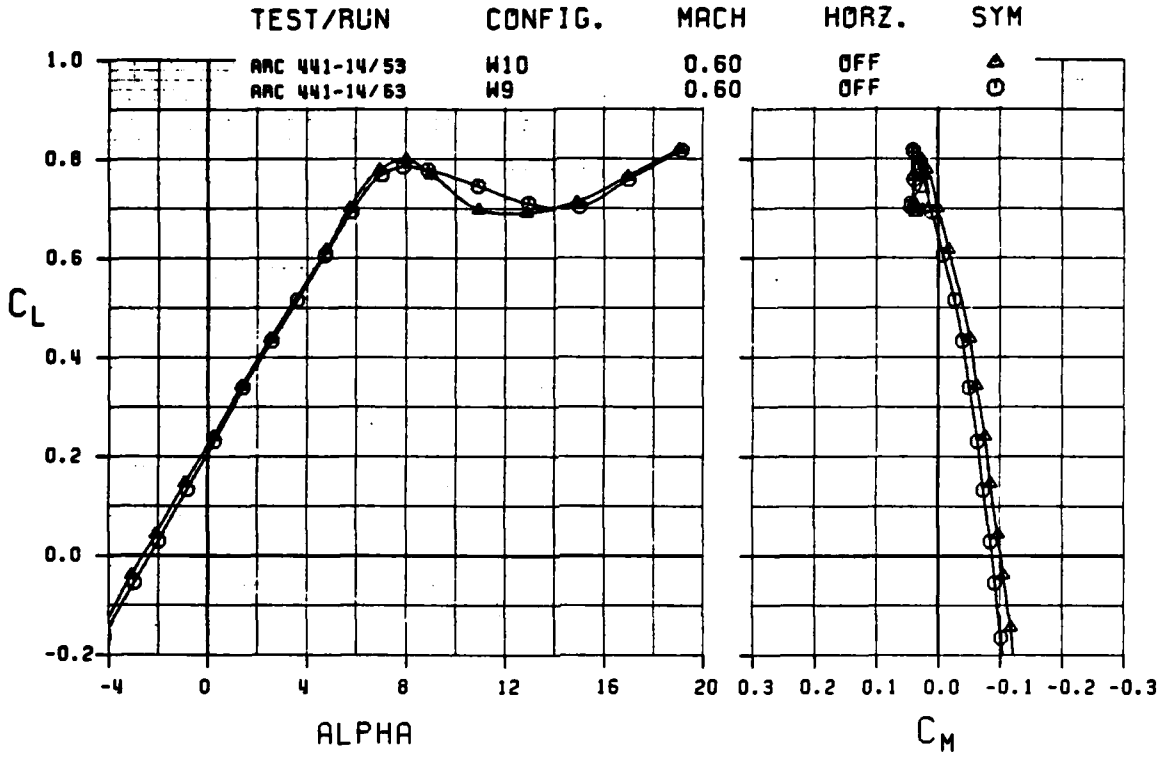

Figure 11 Lift and moment comparison of wings W9 and W10 at M_∞ =0.60.

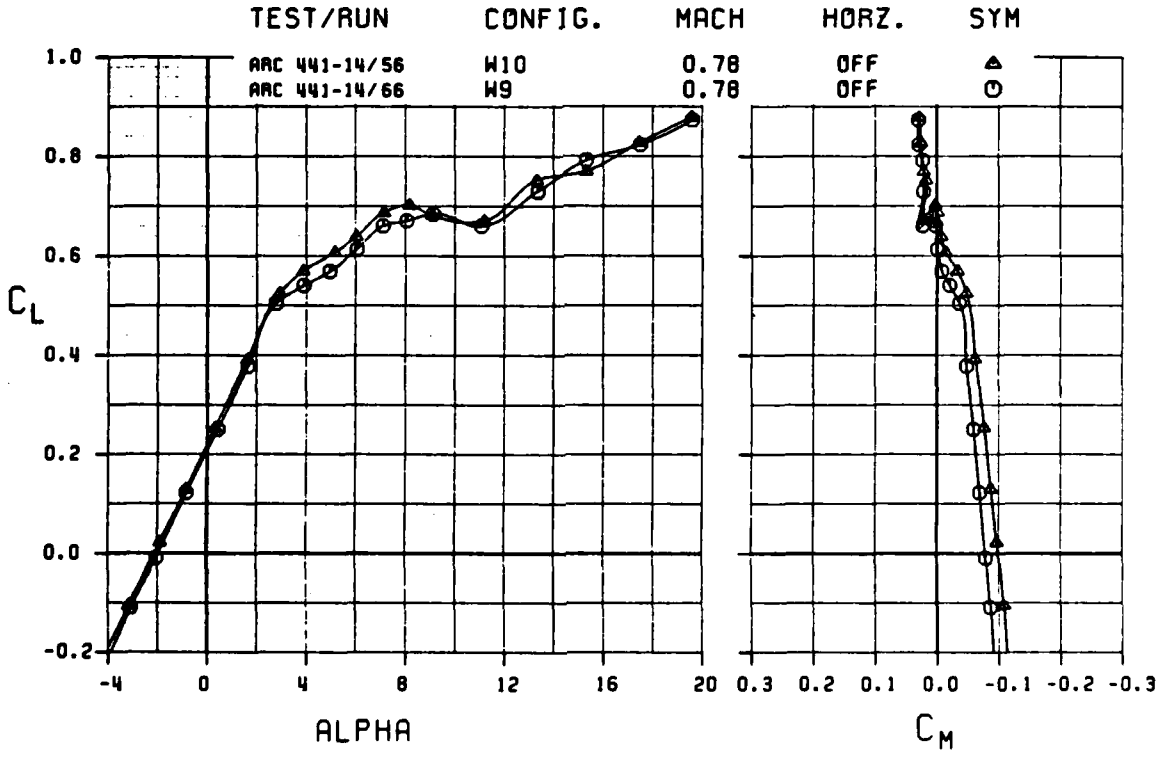

Figure 12 Lift and moment comparison of wings W9 and W10 at M_∞ =0.78.

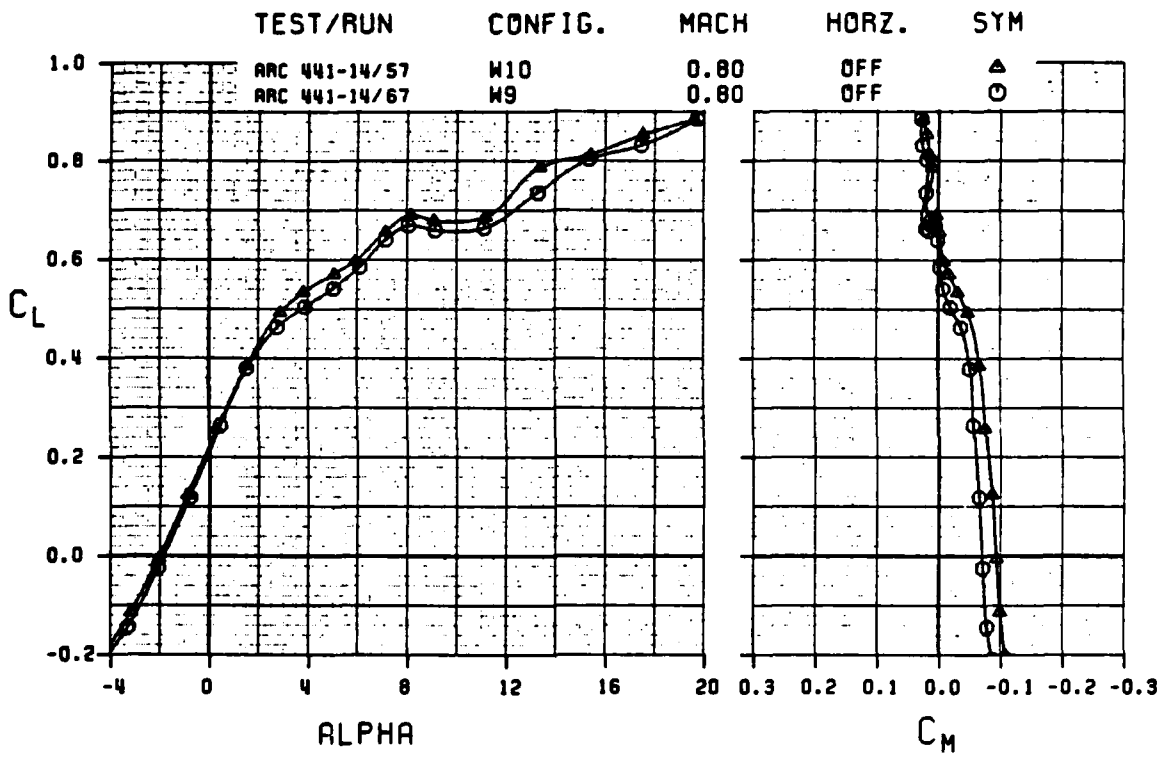

Figure 13 Lift and moment comparison of wings W9 and W10 at M_∞ =0.80.

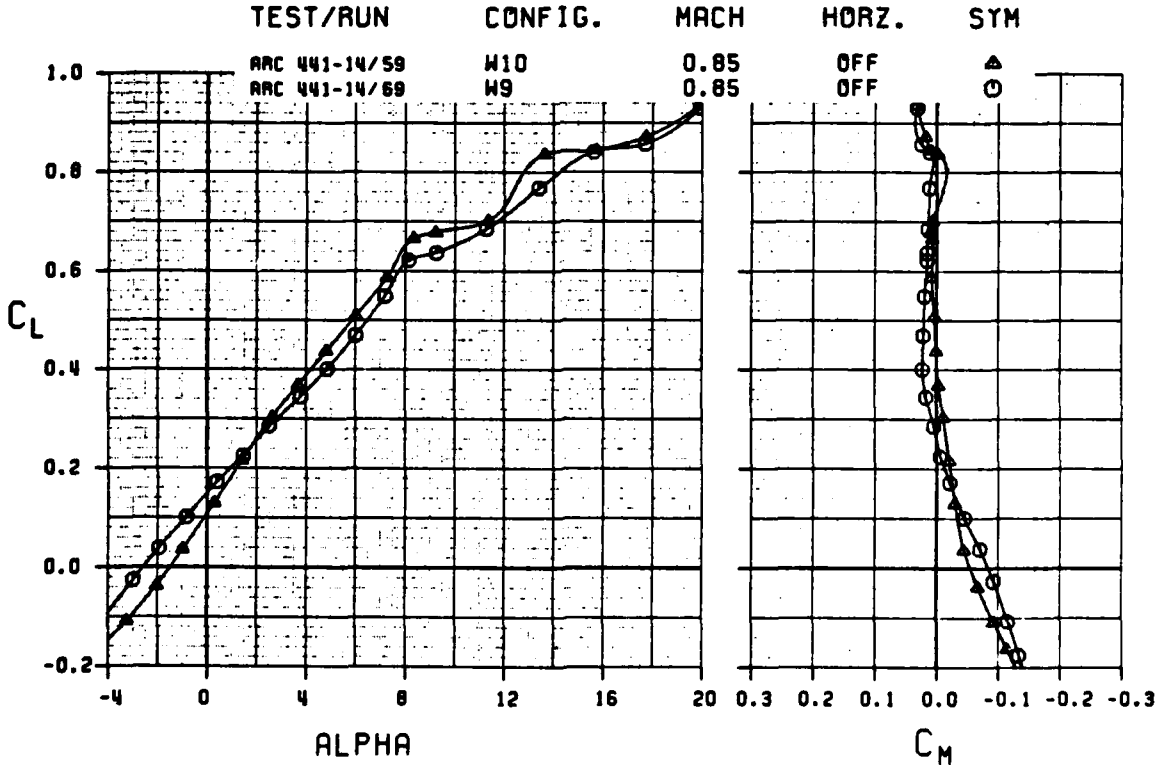

Figure 14 Lift and moment comparison of wings W9 and W10 at M_∞ =0.85.

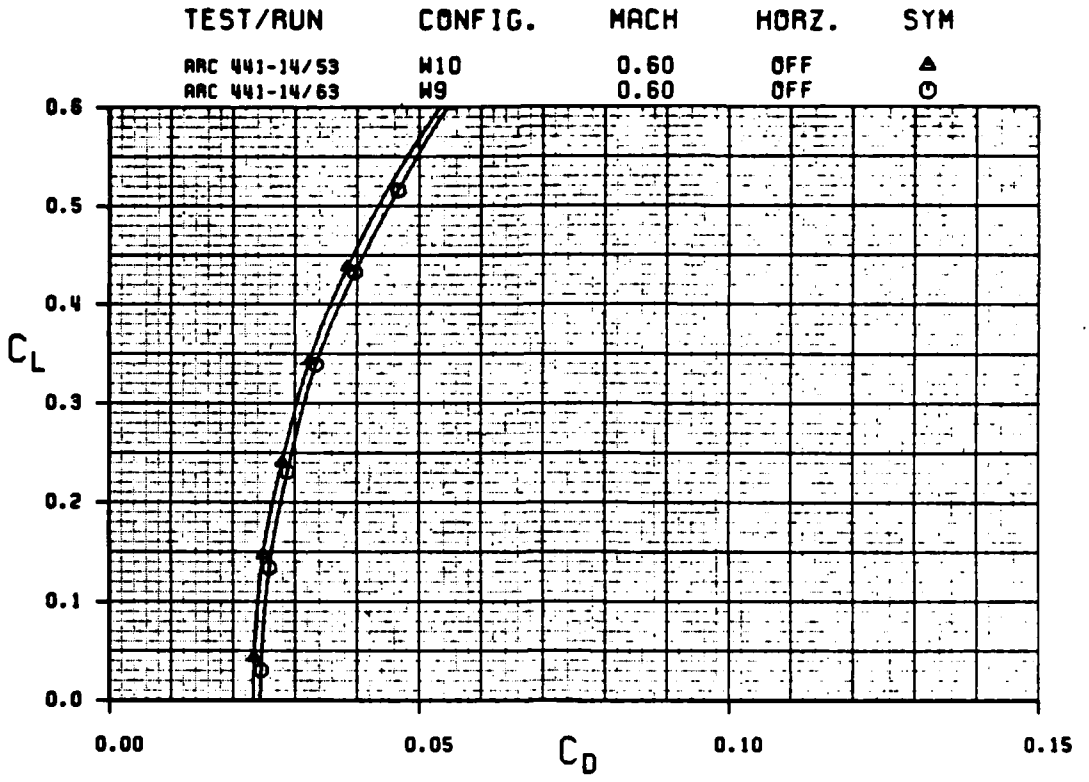

Figure 15 Drag comparison of wings W9 and W10 at M_∞=0.60.

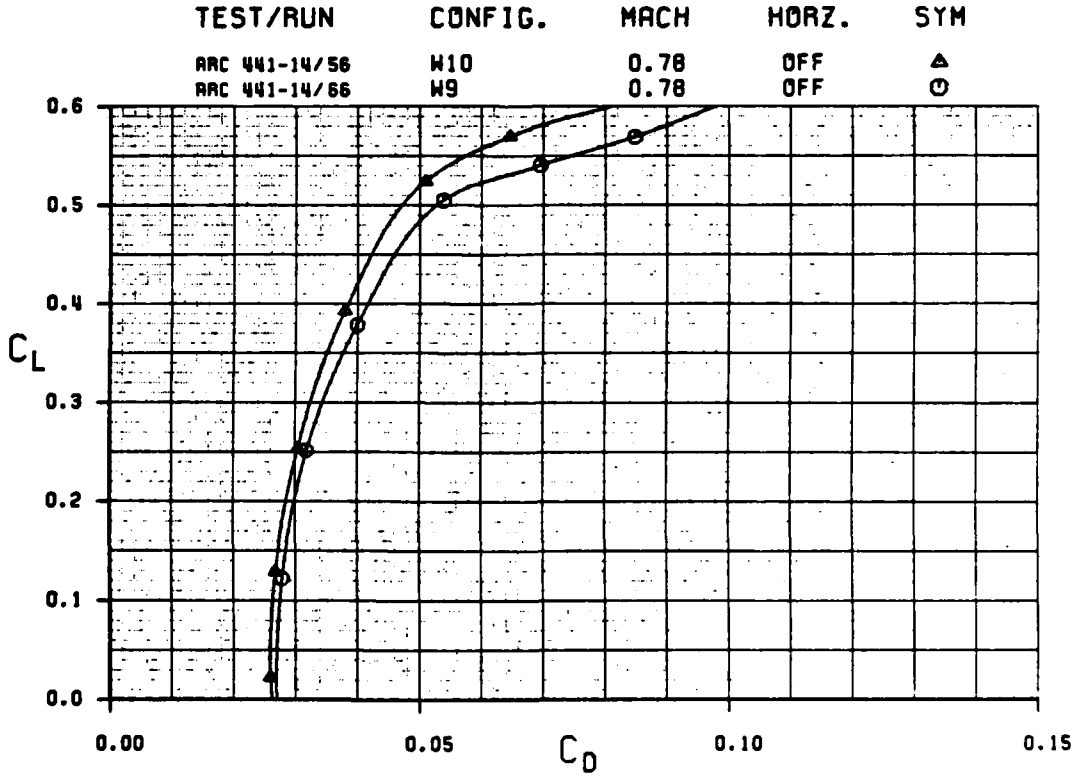

Figure 16 Drag comparison of wings W9 and W10 at M_∞=0.78.

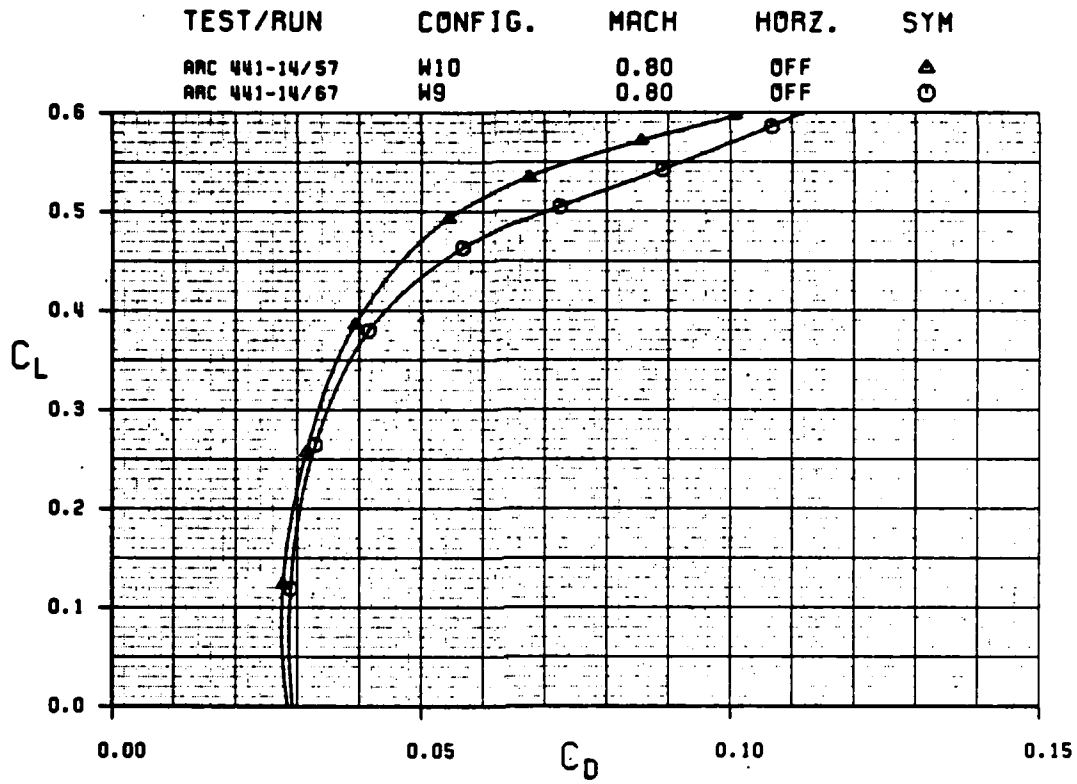

Figure 17 Drag comparison of wings W9 and W10 at M_∞=0.80.

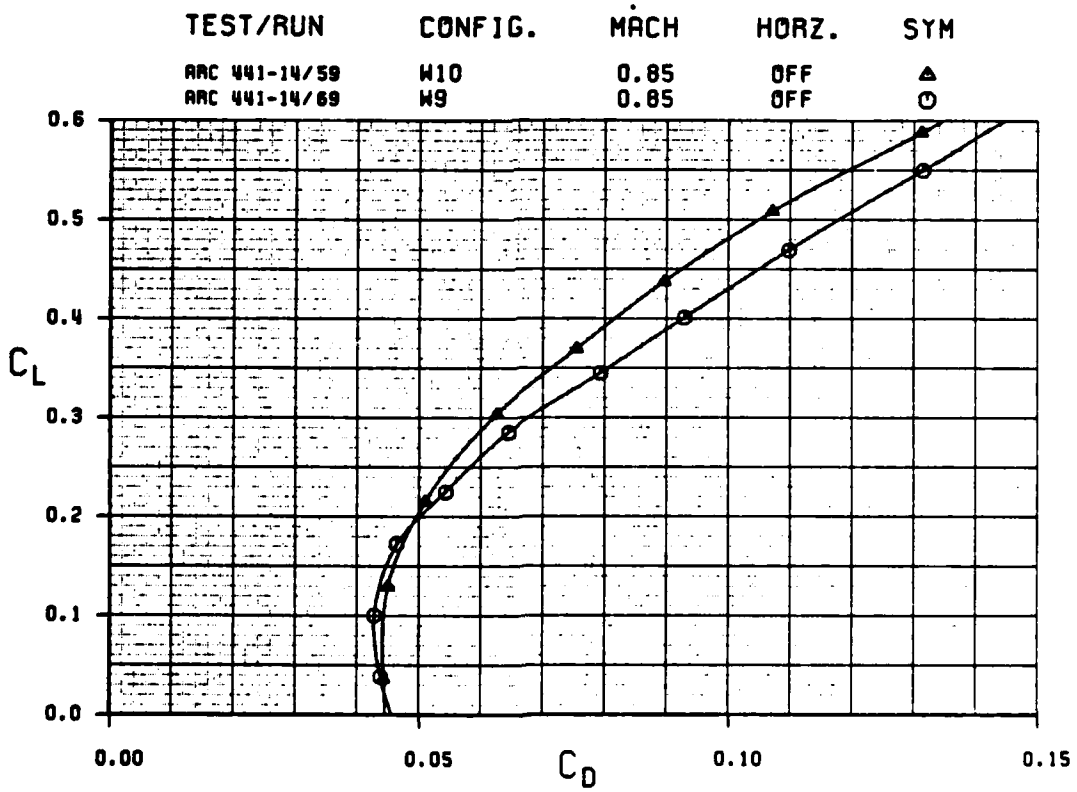

Figure 18 Drag comparison of wings W9 and W10 at M_∞=0.85.

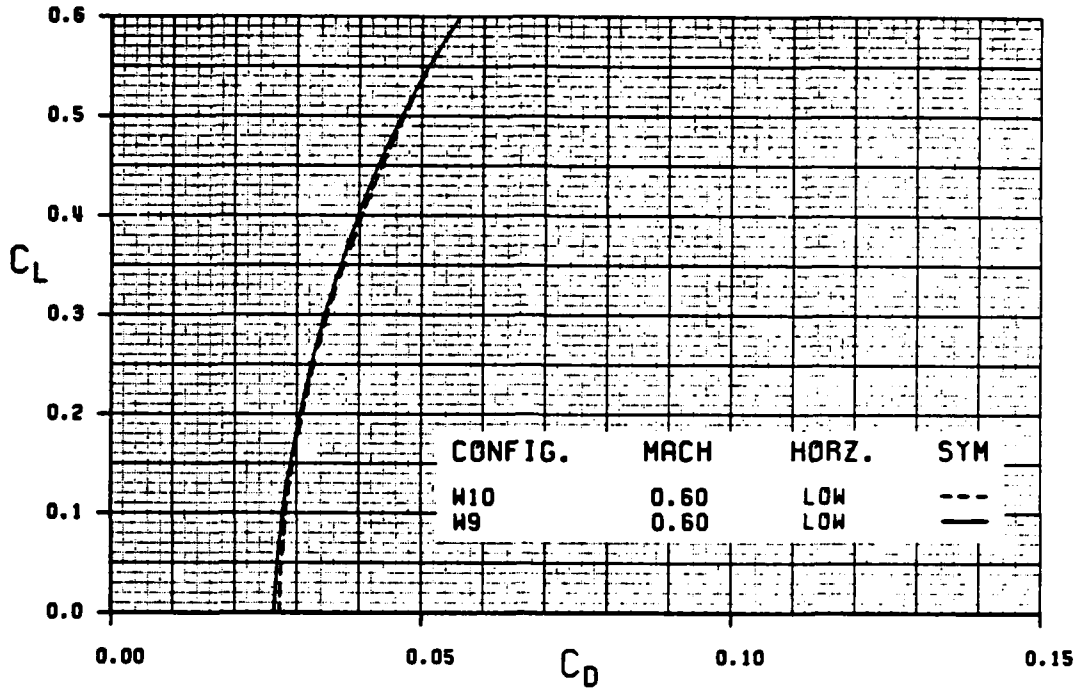

Figure 19 Trimmed drag comparison of wings W9 and W10 at M_∞ =0.60.

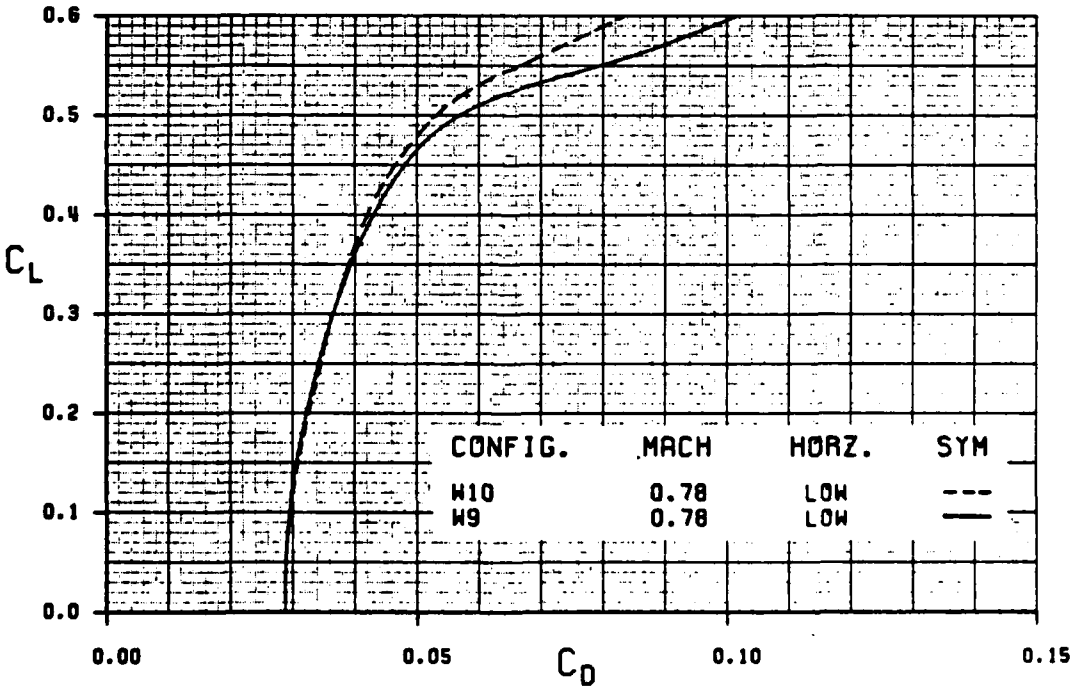

Figure 20 Trimmed drag comparison of wings W9 and W10 at M_∞ =0.78.

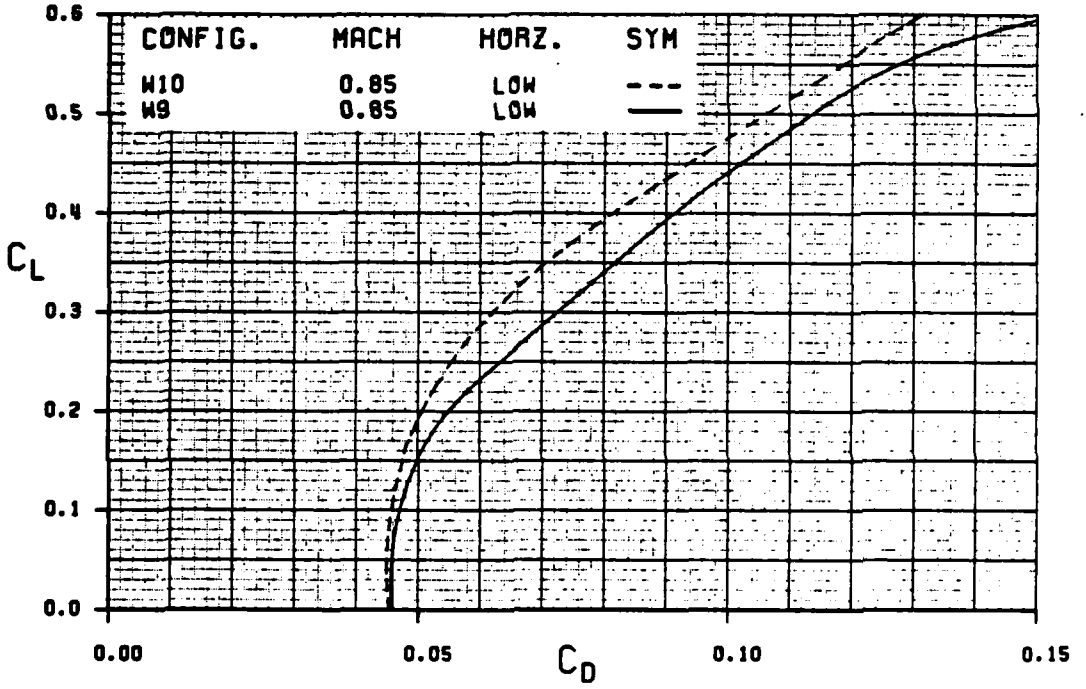

Figure 21 Trimmed drag comparison of wings W9 and W10 at M_∞=0.85.

3.2.2 Wing Pressure Distribution Analysis

The cause of the early drag rise of wing W9 over that of W10 for the wing-alone case can be perceived by a comparison of the pressure distributions from the two wings. It is observed in Figure 22 that wing W10 has reduced leading-edge pressure, a more aft shock location, and a slightly weaker shock than wing W9. Additionally, wing W10 has a small lift increment over W9 on the lower surface. While these slight changes may account for a portion of the difference in drag rise, the main factor contributing to the drag is the requirement of an increased angle of attack for W9 to obtain a given C_L. (See for example Figure 13 at C_L=0.5.) The angle of attack required to obtain the C_L increment results in trailing-edge separation for the M_∞=0.80/C_L=0.50 case.

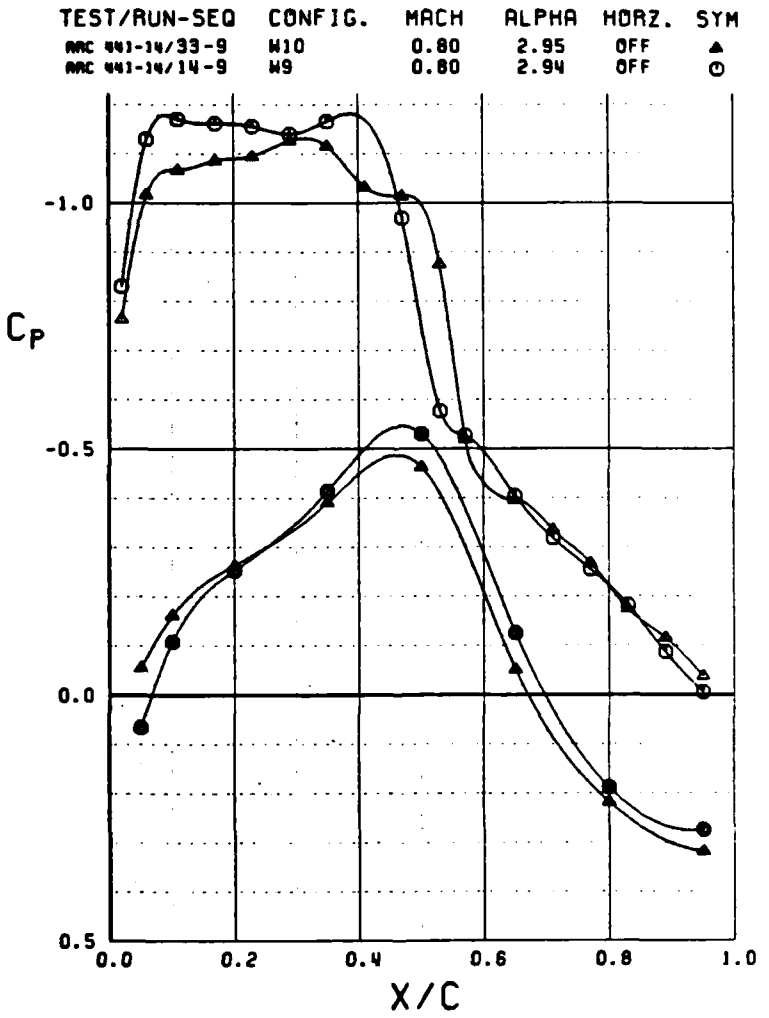

Figure 22 Comparison of wing W9 and W10 pressures.

The effect of a change in airfoil curvature is observed in Figure 23. Rapid slope changes, leading into the cusp of wing W9, were reduced on wing W10. The result is a reduction in the cusp pressure gradient for high Mach number/low C_L conditions.

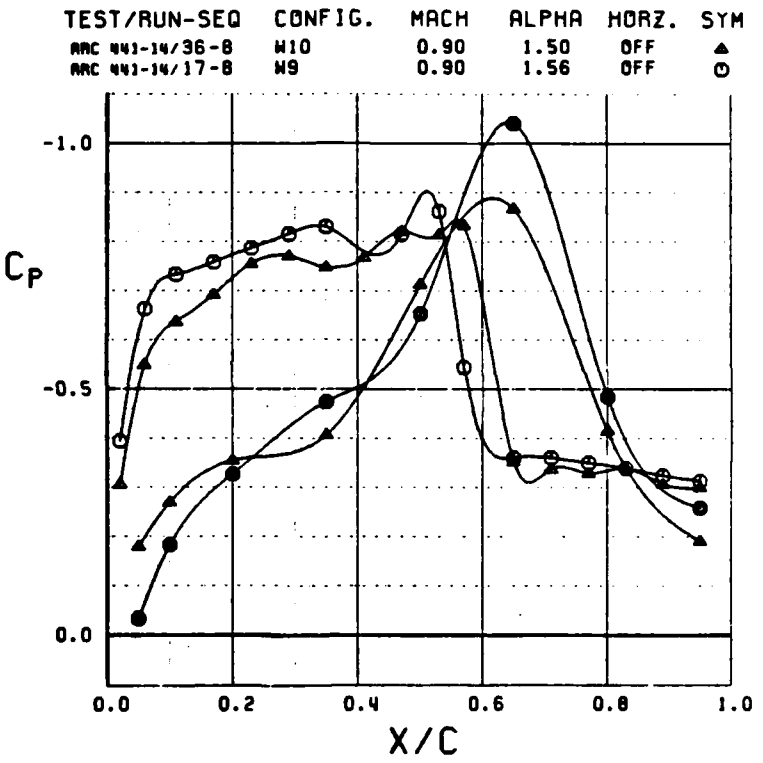

Figure 23 Change in cusp pressures between wings W9 and W10.

3.2.3 Oil Flow Results

Photographs of oil flow runs on wings W9 and W10 are shown in Figure 24 for M_∞=0.78 and for angles of atack of 2, 3, 4, and 6 deg. The wing pressures corresponding to the oil flow runs are presented in Figures 25 for α=2 and 3 deg and in Figure 26 for 4 and 6 deg.

For α=2 deg, a smeared shock is visible on wing W10. Outboard of the pressure row the shock strength remains roughly constant. However, on wing W9 the shock strength increases and unsweeps toward the leading edge of the tip. The shock location remains aft on W10 and diffuses out near the tip.

At α=3 deg, the shock intensity increases across the entire span for both wings. However, the shock remains smeared over approximately 5 percent of the chord inboard of the pressure row.

As angle of attack is increased to 4 deg, the first signs of separation are visible (directly outboard of the pressure row). This concurs with the break in C_L-α between 3 and 4 deg as seen in Figure 12.

At α=6 deg, separated flow envelopes the majority of both wings. The tip shock for wing W9 is still significantly stronger than on W10.

Figure 27 displays an oil flow pattern over the lower surface of wing W9 at α=2 deg. A significant amount of spanwise flow is observed in the cusp.

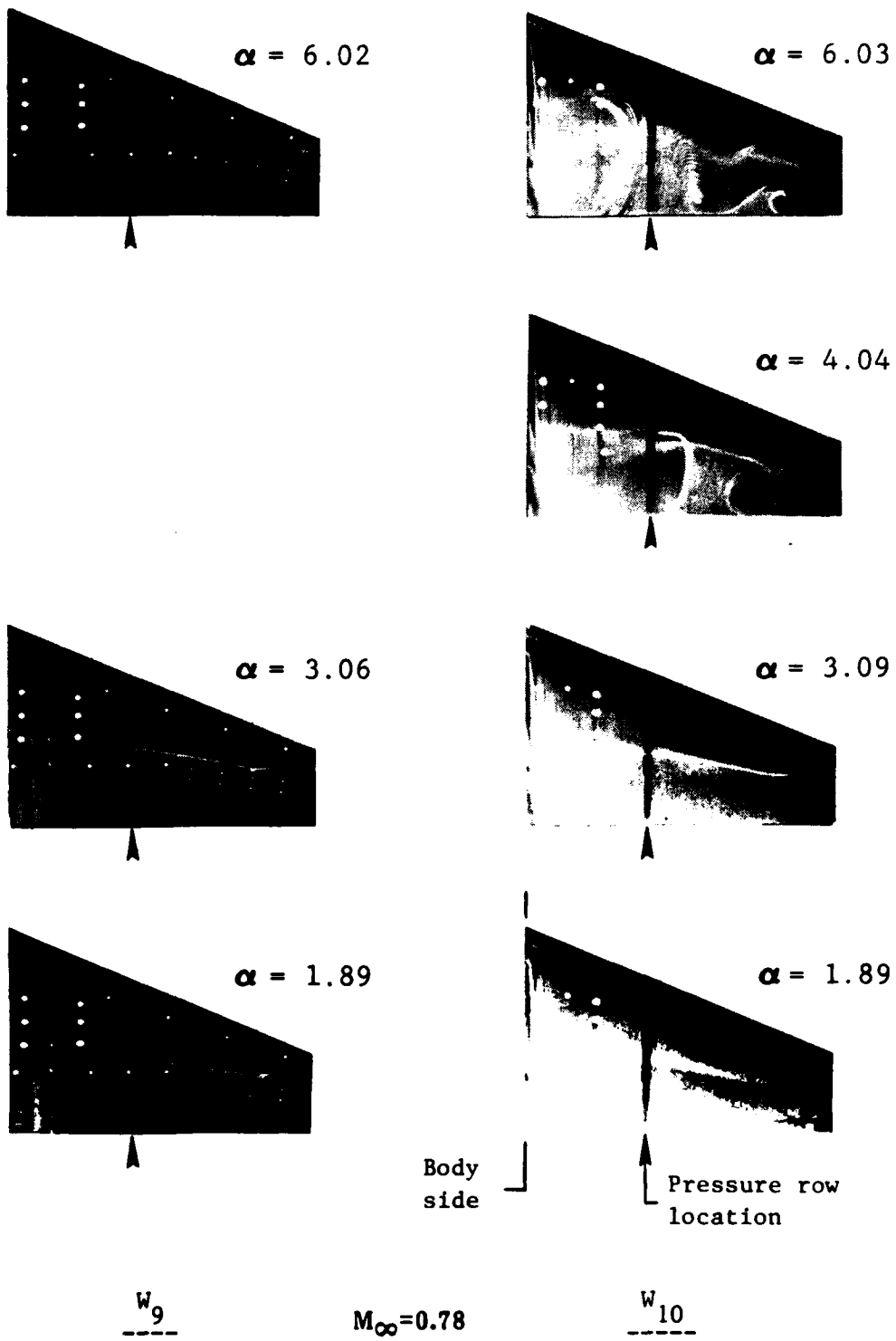

Figure 24 Oil flow photographs of wings W9 and W10.

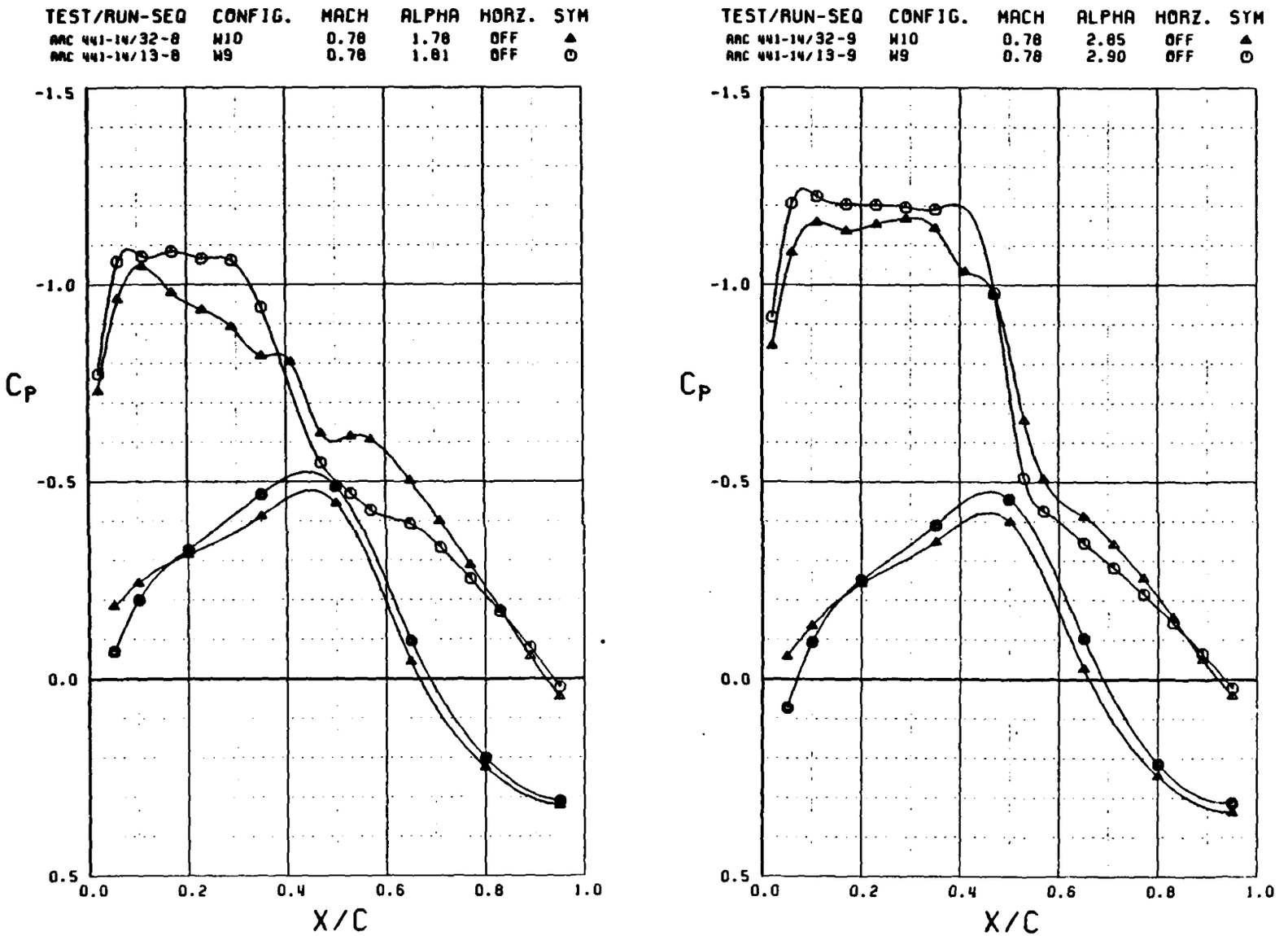

Figure 25 Wings W9 and W10 pressures at M_∞=0.78/α=2° and 3°.

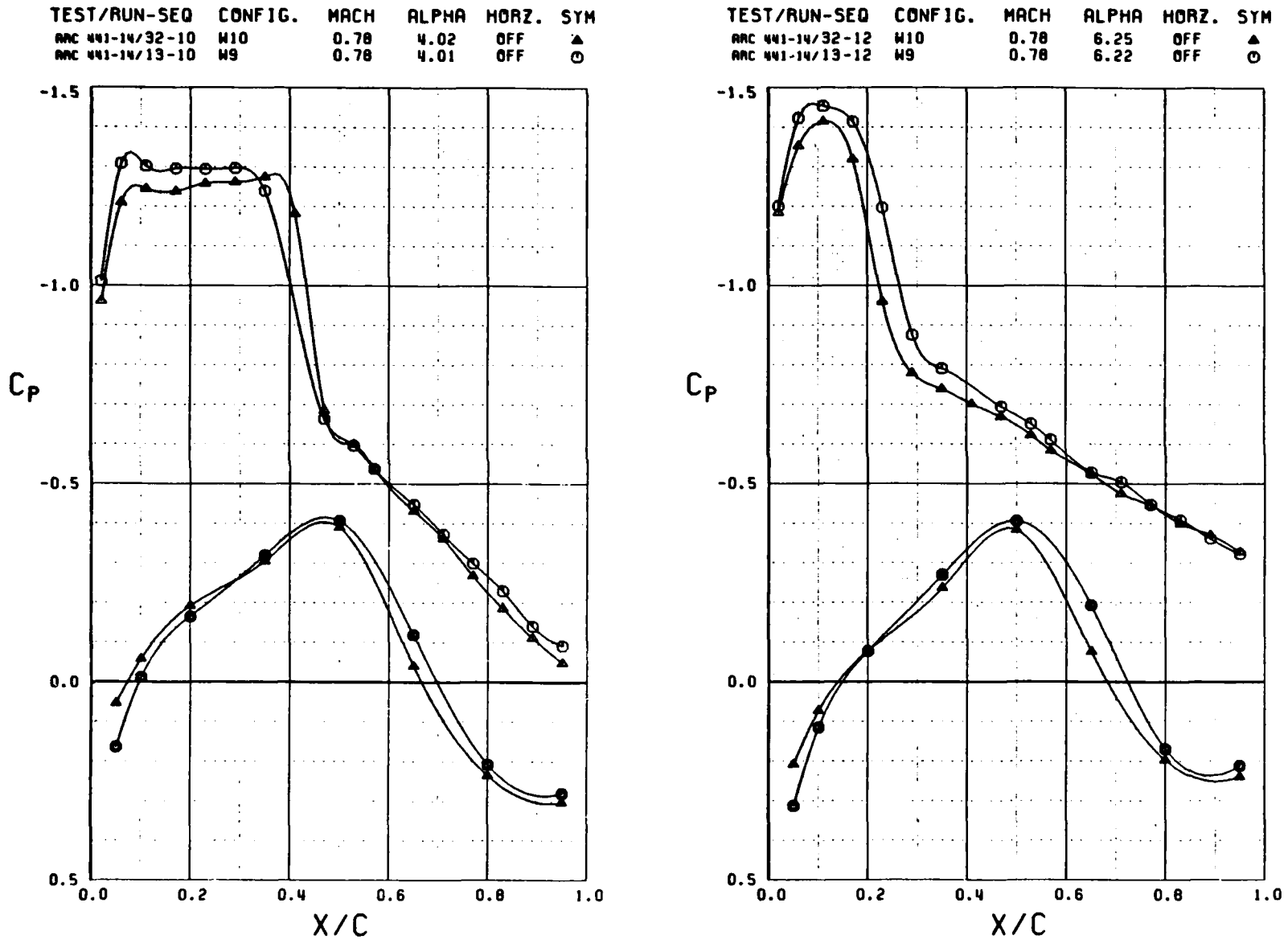

Figure 26 Wings W9 and W10 pressures at $M_\infty = 0.78/\alpha = 4°$ and $6°$.

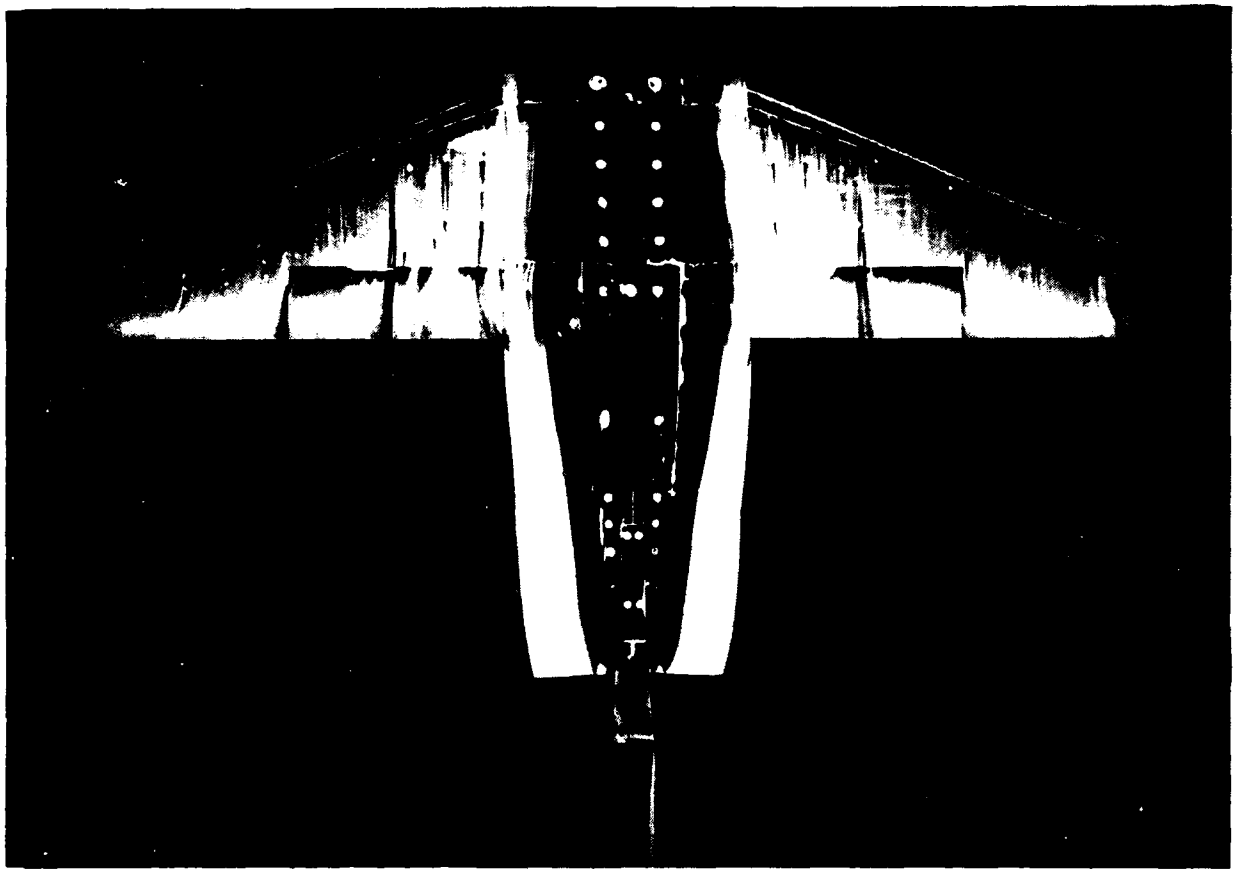

Figure 27 Oil Flow photograph of the lower surface of wing W9.

3.3 HORIZONTAL TAIL CHARACTERISTICS

Horizontal tail data were acquired at Mach numbers of 0.60, 0.78, and 0.85 and at tail deflections of -10, 0, and +10 deg.

A more extensive tail test-series was run with wing W9 than with W10, so the following discussion details the results obtained with wing W9 on the model. The force data acquired includes the low-tail at deflections of -10, 0, and +10 deg, the mid-tail at -10 and 0 deg, and the T-tail at -10 and 0 deg. Pressure data were obtained for all of the force configurations except for the T-tail at -10 deg.

3.3.1 Horizontal Tail Effectiveness

C_L-α and C_L-C_M data for the low-, mid-, and T-tail are presented in Figures 28, 29, and 30, respectively, for a freestream Mach number of 0.78. A stable break in pitching moment occurs when the wing stalls. As angle of attack is increased further, the mid-and T-tails exhibit an unstable trend. The pitching moment curve for the wing-alone condition is shown in Figure 28.

Evaluation of the pitching moment data indicates a moment change with respect to tail deflection (C_{m_δ}) of approximately - 0.025 at M_∞=0.78 for the low- and T-tails with attached flow. This value of C_{m_δ} was computed using the low-tail data for $\alpha < 4$ deg and tail deflections of 0 and +10 deg and the T-tail data for $\alpha > 12$ deg and tail deflections of 0 and -10 deg. For the angle of attack and tail deflections listed, the wing-alone pitching moment data lie between the two tail deflections, which indicates local tail angles-of-attack of less than 10 deg. The horizontal tail lift curve slope is assumed to be linear in this region. The T-tail data were ratioed by the moment arms (0.30 wing C_{mac} to 0.25 tail C_{mac}) of the two tails.

For the -10 deg tail deflections a decrease in C_{m_δ} is observed for all three tail locations. The reductions in tail effectiveness are attributed to non-linearities in the tail lift curve slope due to flow separation. The most significant reduction in C_{m_δ} occurrs for the mid-tail. This may be caused by a local flow acceleration on the upper surface of the nacelle/body when the tail is at a negative angle of attack to the flow. Approximate values of downwash (ϵ), at the three tail locations, are presented

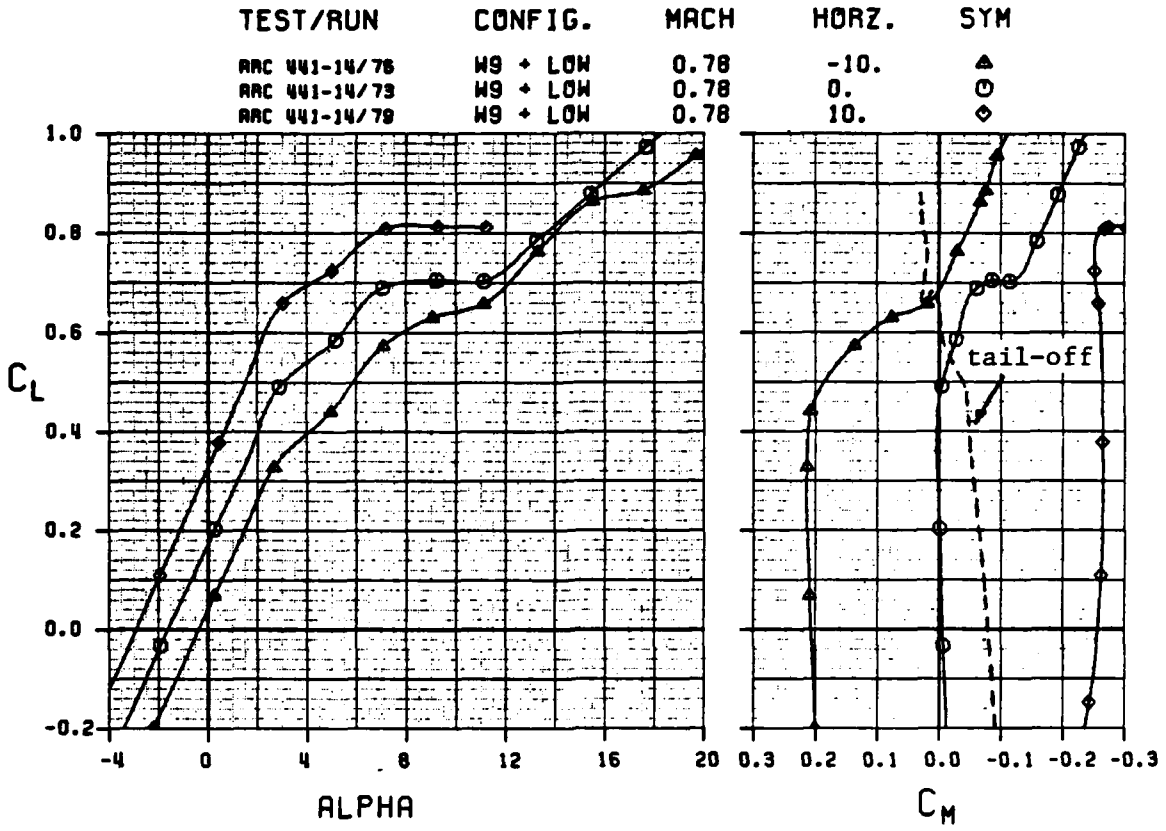

Figure 28 Lift and moment data for the low-tail configuration at M_∞ =0.78.

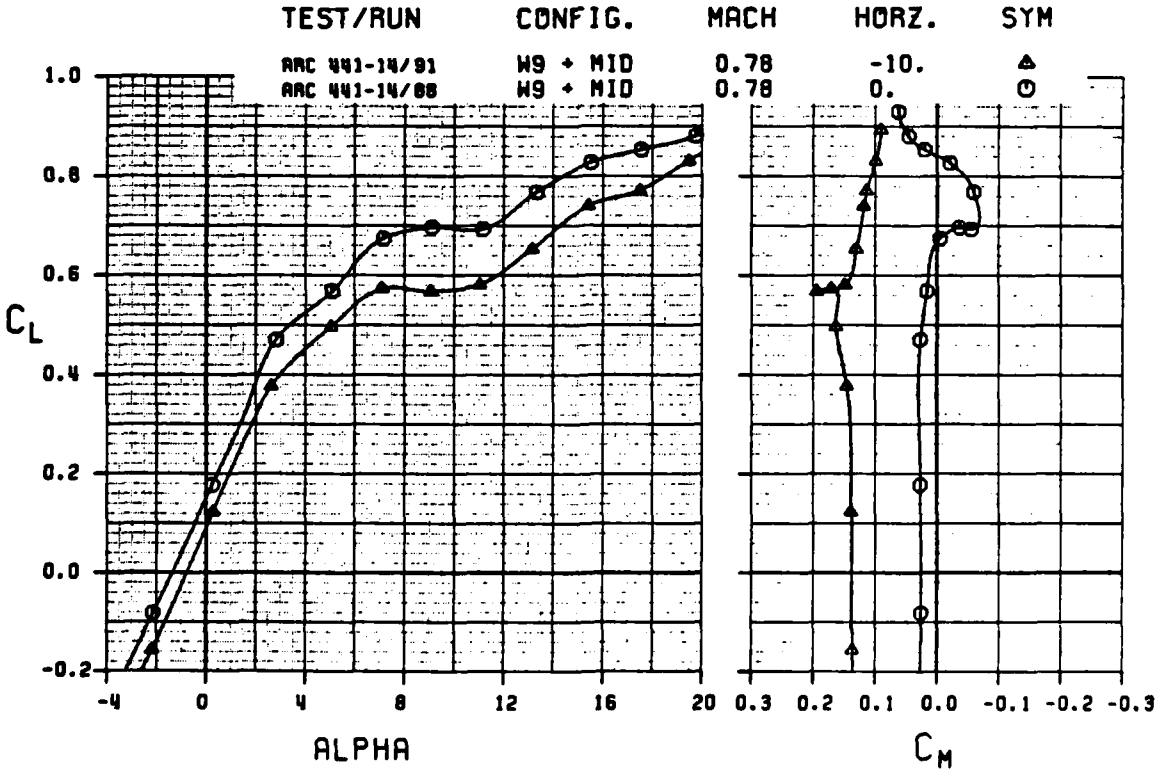

Figure 29 Lift and moment data for the mid-tail configuration at M_∞ =0.78.

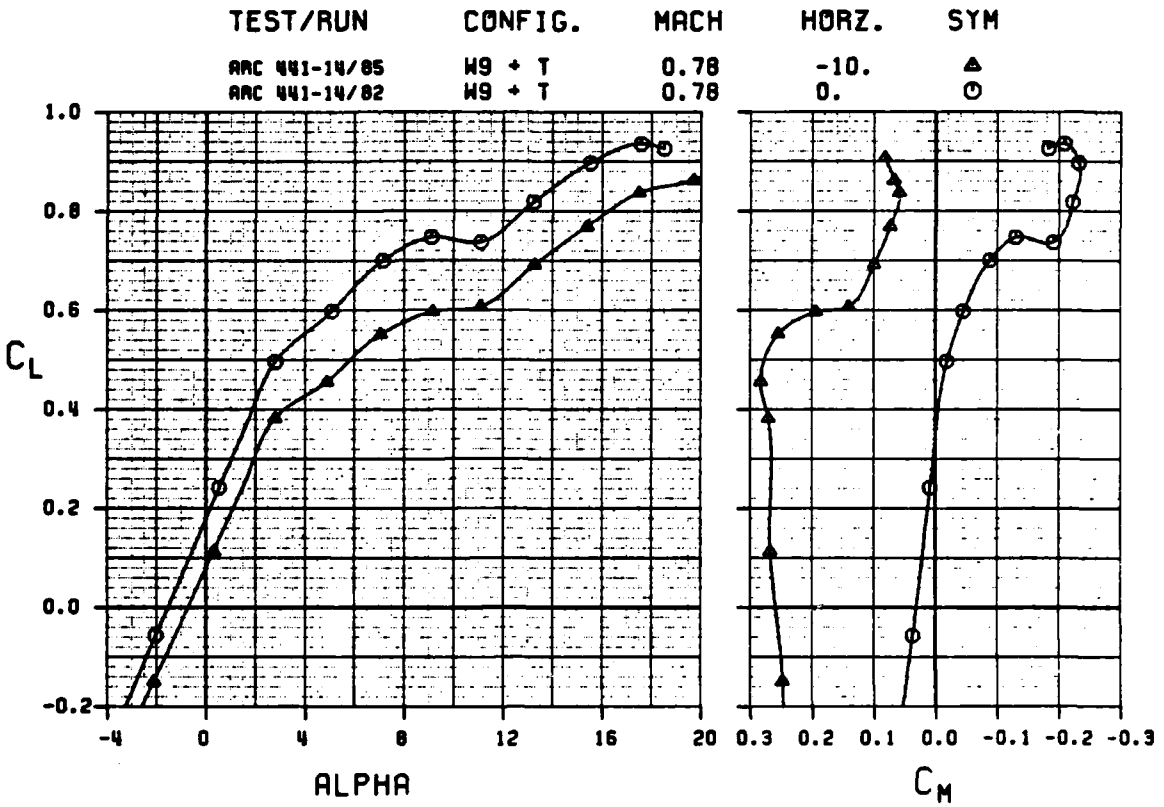

Figure 30 Lift and moment data for the T-tail configuration at M_∞ =0.78.

in Figure 31. The assumptions made in the calculations are: a) The local downwash, ϵ, is equal to the sum of the configuration angle of attack and the horizontal tail deflection necessary to equate the tail-on configuration pitching moment to the tail-off moment, and b) C_{m_δ} equals -0.025 for the tail in the deflection range between the δ_H=0 deg moment curve and the tail-off curve.

The downwash at the three tail locations remains linear until near the angle of attack at which the wing stalls. The change in downwash with angle of attack, ϵ_α, is largest for the low-tail ($\epsilon_\alpha \approx 0.8$), slightly less for the mid-tail ($\epsilon_\alpha \approx 0.7$), and lowest at the T-tail ($\epsilon_\alpha \approx 0.4$). A value of ϵ_α of 0.78 is predicted using the vortex theory method presented in Reference 4, which assumes an elliptical lift distribution.

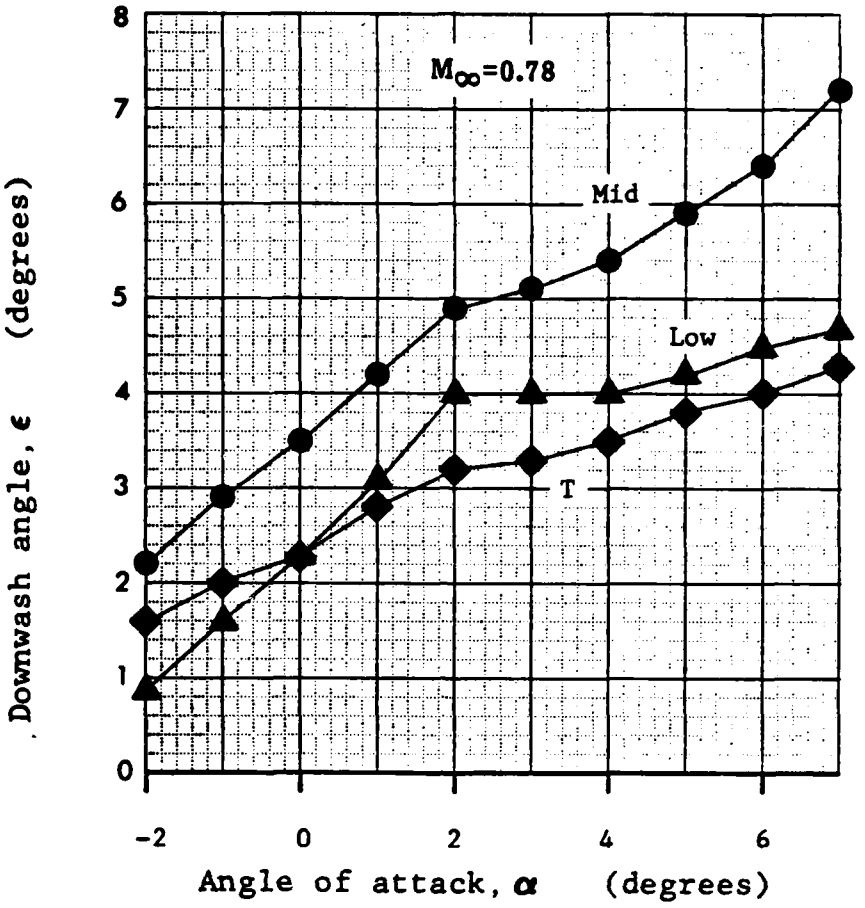

Figure 31 Downwash at the low-, mid-, and T-tails.

While the values of ϵ_α for the three tail locations are reasonable, the differences in downwash between the tails, at a specific angle of attack, appear different from what is generally expected. The downwash at the T-tail location should be less than at the low-tail location for a wing-alone configuration. The discrepancy observed in Figure 31 may be a body effect but most probably it is due to the fact that the spanwise extension of the low-tail (mounted on the nacelle) is considerably greater than for the T-tail.

The large downwash values observed for the mid-tail are probably caused by entrainment of the flow on the upper surface of the body. The complexity of the flow in the mid-tail region may render the approximations made in the downwash calculations invalid.

Figures 32 and 33 present the lift and moment data for the low-tail at M_∞=0.60 and 0.85. Only small differences in tail effectiveness occur.

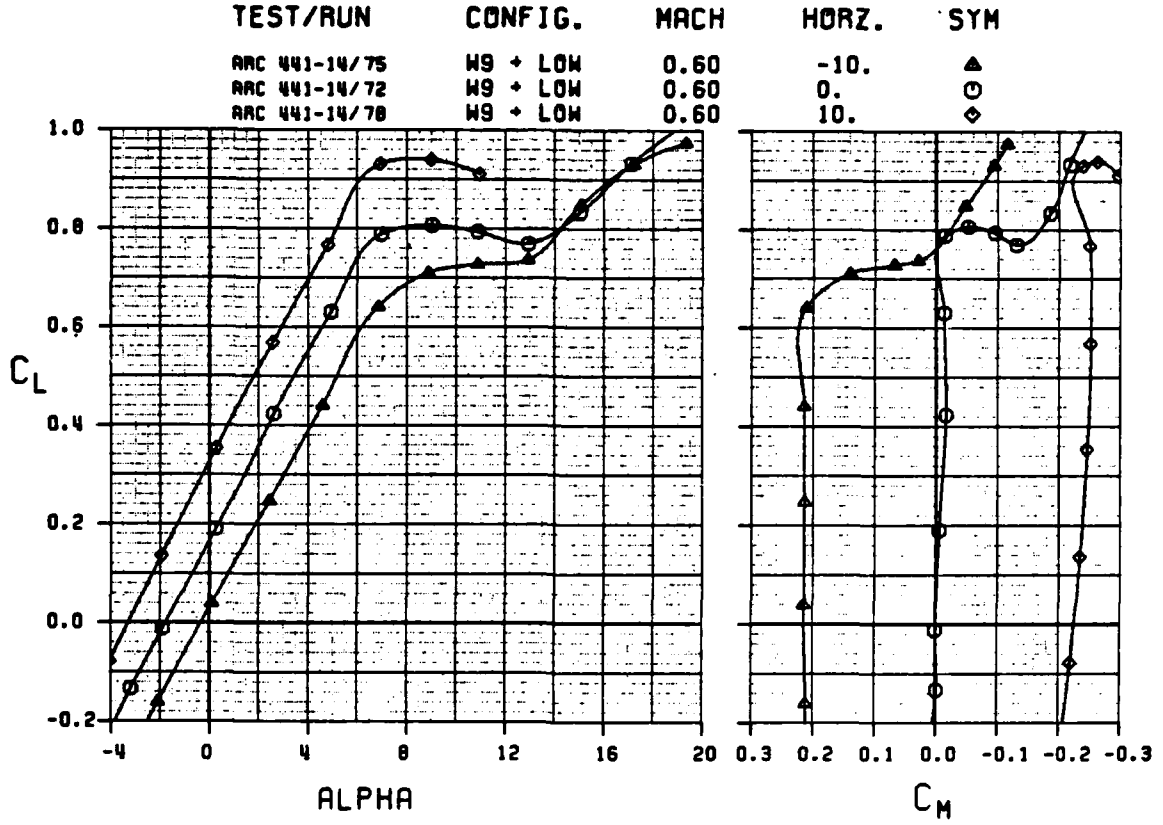

Figure 32 Lift and moment data for the low-tail configuration at M_∞ =0.60.

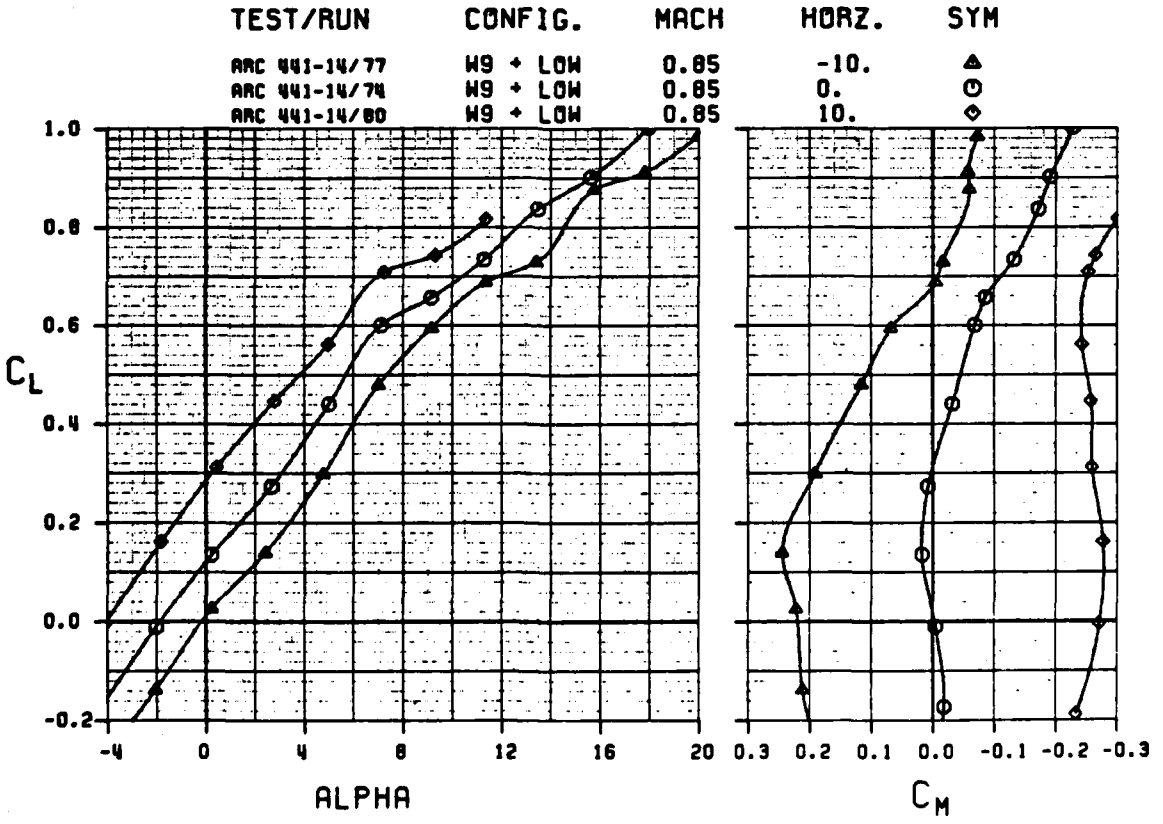

Figure 33 Lift and moment data for the low-tail configuration at M_∞ =0.85.

3.3.2 Tail Effects on Configuration Forces

Trimmed lift and drag data for model 603E are presented in Figures 34 and 35 for the low-, mid-, and T-tail configurations at M_∞ =0.78. Only slight differences in the lift data are observed. The low-tail configuration has slightly lower drag than the T-tail for $C_L < 0.5$. In the C_L range 0.5 to 0.6 the T-tail has approximately 60 counts less drag than the low-tail. Below C_L=0.5, the trimmed drag of the mid-tail configuration was computed to be slightly higher than for the low- or T-tail configurations.

Accurate trimmed drag predictions above C_L=0.6 are not possible because of the limited number of tail deflections tested. Since only two deflections were available to develop the trimmed polars for the mid- and T-tail configurations, the significance of the differences in drag cannot be rigorously substantiated.

3.3.3 Horizontal Tail Pressure Distribution Analysis

Data for the low-, mid-, and T-tails at M_∞ =0.78, α =0.5 deg, and δ_H=0 deg are presented in Figure 36. The tail planform and flight conditions remain virtually unchanged between the three positions, yet noteable differences in the pressures are observed. These differences are attributed to dynamic pressure reductions downstream of the wing, local differences in downwash angle, and interference effects.

Figures 37 and 38 present data for the three tail positions at M_∞ =0.78 and 0.85, respectively, at local angles of attack of approximately 0 deg. A dashed line is drawn on each distribution to indicate the assumed pressure distribution at exactly zero degrees angle of attack. The low-, mid-, and T-tail pressures at M_∞ =0.78 have similar shapes. However, the peak pressures on the tails (near 35% chord) differ for each. The mid-tail exhibits the lowest peak pressure ($C_p \approx -0.5$) and the low-tail the highest ($C_p \approx -0.3$).

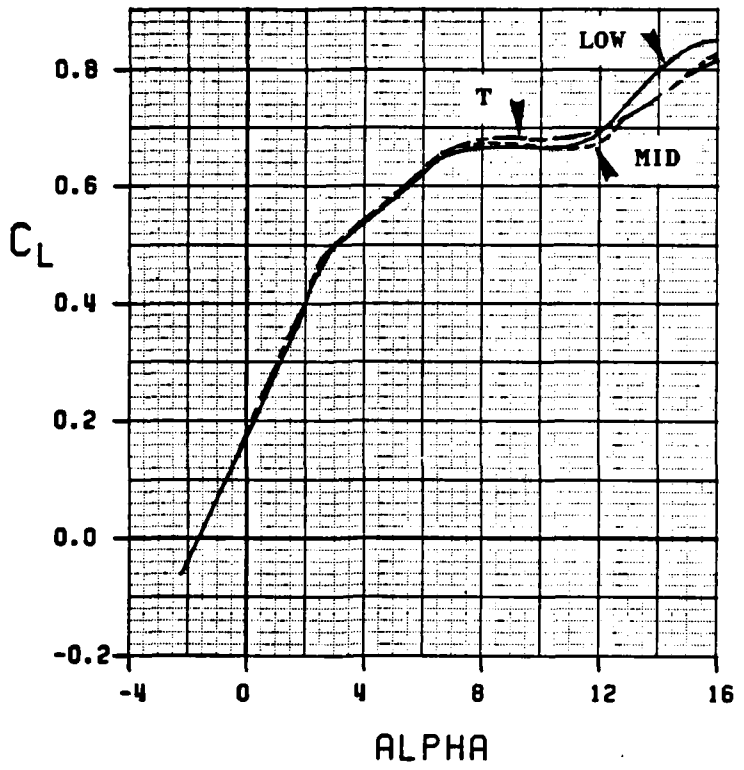

Figure 34 Low-, mid-, and T-tail configuration trimmed lift curves at M_∞ =0.78

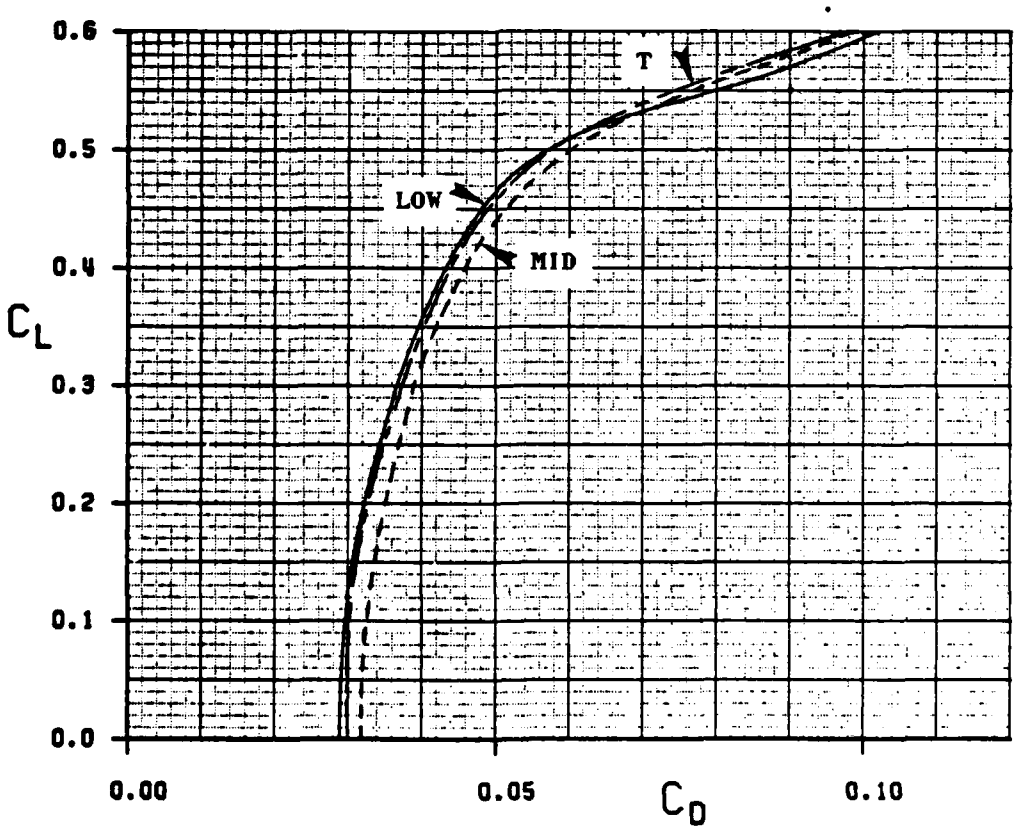

Figure 35 Low-, mid-, and T-tail configuration trimmed drag polars at M_∞ =0.78.

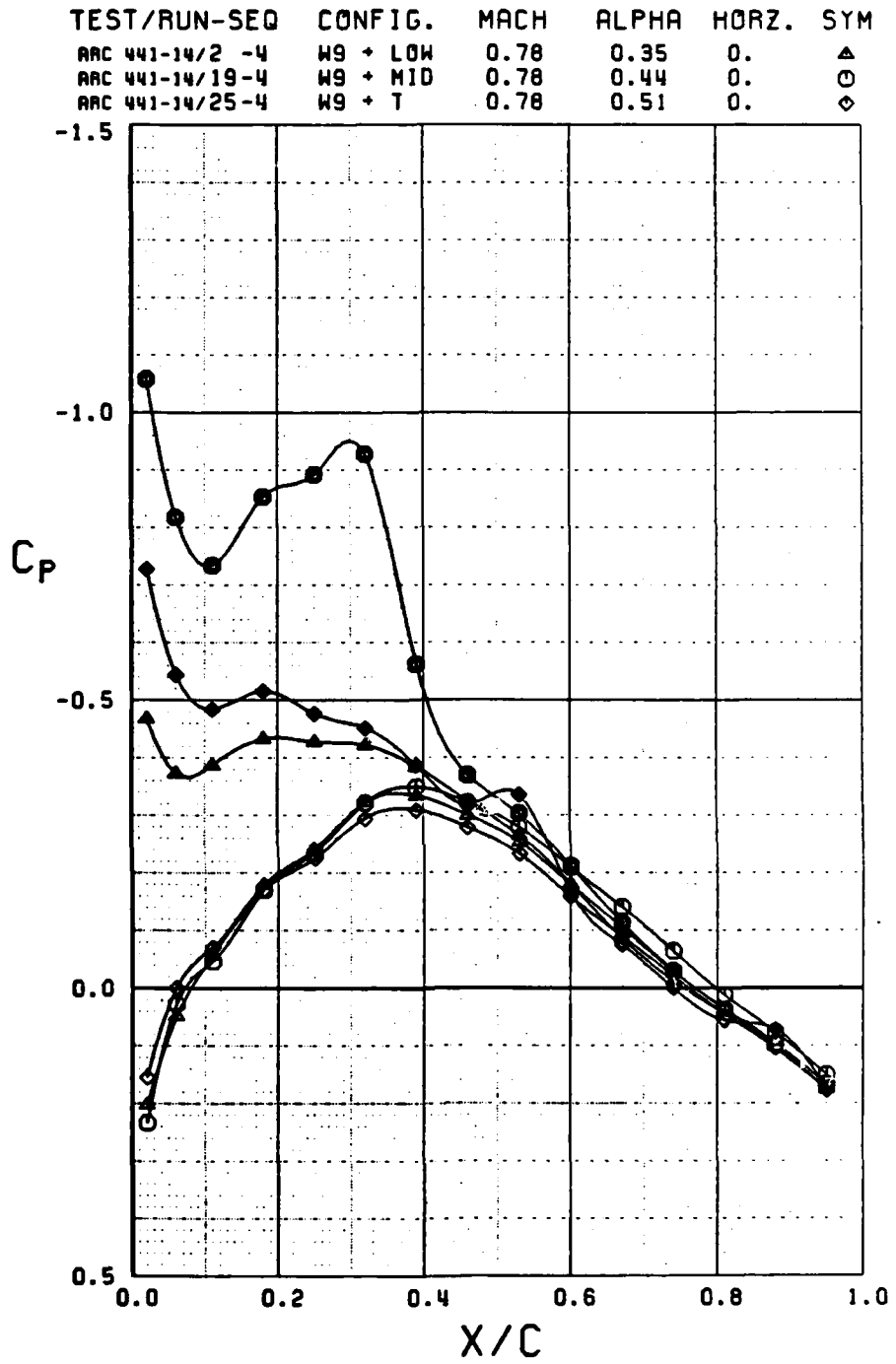

Figure 36 Horizontal tail pressures at M_∞=0.78, α=0.5 deg, δ_H=0 deg.

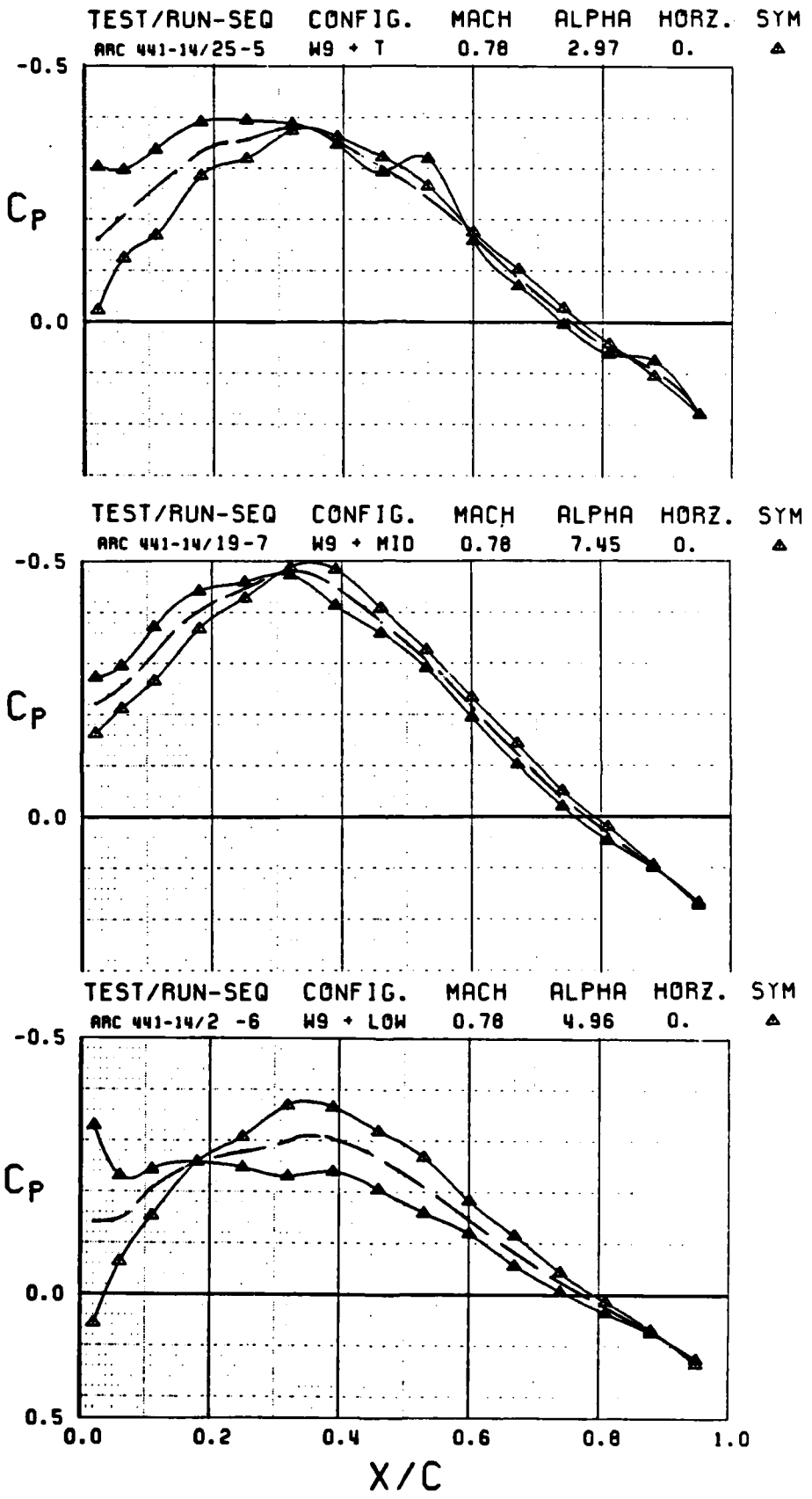

Figure 37 Tail location effects at M_∞=0.78.

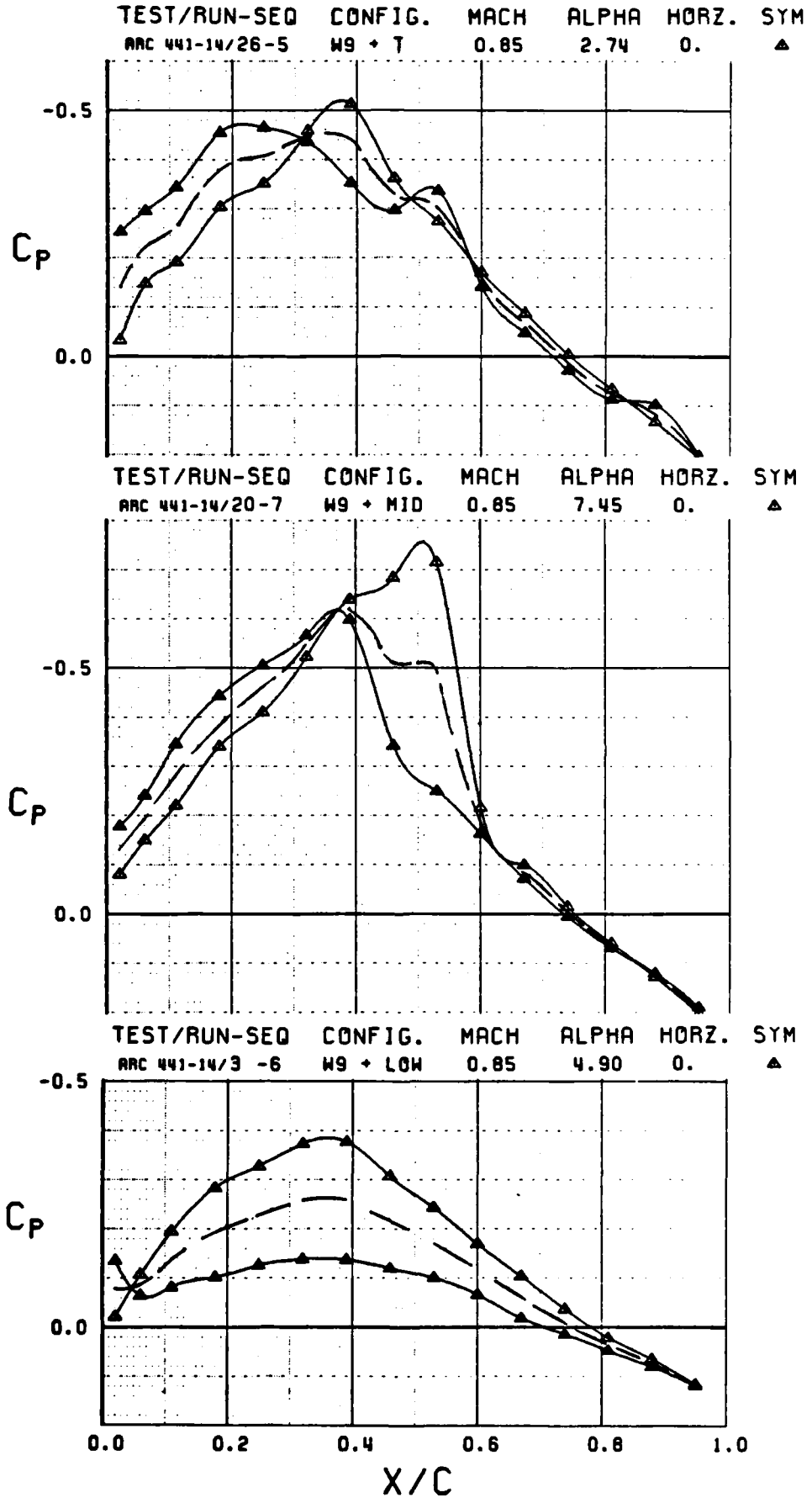

Figure 38 Tail location effects at M_∞=0.85.

For a Mach number of 0.85 (see Figure 38) the pressure near the mid-chord of the tail airfoil section remains virtually unchanged for the low-tail and decreases slightly for the T-tail. The flow acceleration on the mid-tail results in a shock formation near mid-chord. This early shock formation is considered to be the key factor in the drop in the mid-tail's effectiveness. It is suspected that the combined interference of the horizontal tail, the vertical tail, and the body is forcing a local flow acceleration in the region below the mid-tail.

The high pressures observed near mid-chord on the low-tail (Figures 37 and 38) are attributed to a drop in dynamic pressure in the wing wake. As the low-tail passed out of the wake, improved results were observed.

Figure 39 shows a comparison of low- and T-tail pressures at a local angle of attack of -3.4 deg (derived based on the downwash curves of Figure 31). The good agreement between the pressures on the upper surface helps verify the downwash predictions. The discrepancy in the pressures on the lower surface is suspected to be caused by interference effects from the vertical tail on the T-tail lower surface.

Local angle of attack effects on the low-, mid-, and T-tail pressure distributions are presented in Figures 40, 41, and 42, respectively for M_∞=0.78. Similar behavior between the low- and T-tails is observed in that the leading-edge peak pressures develop into a shock located between 10 and 20 percent chord. The pressures initially level off downstream of the shock, followed by a recompression to the trailing edge.

As local angle of attack is increased at the mid-tail, a weak shock appears near 35 percent chord. With increasing angle of attack, high peak pressures near the leading-edge develop into a forward shock. The shock structure for the lower surface is shown because of an inability to get positive local angles of attack for the mid-tail due to the large downwash in that region.

The development of the shock on the low-, mid-, and T-tails with increasing Mach number is observed in Figures 43, 44, and 45. The local angle of attack at the tails is approximately 5 deg. A shock has developed on the upper surface of the mid-tail, at M_∞ = 0.85, in addition to the lower surface shock.

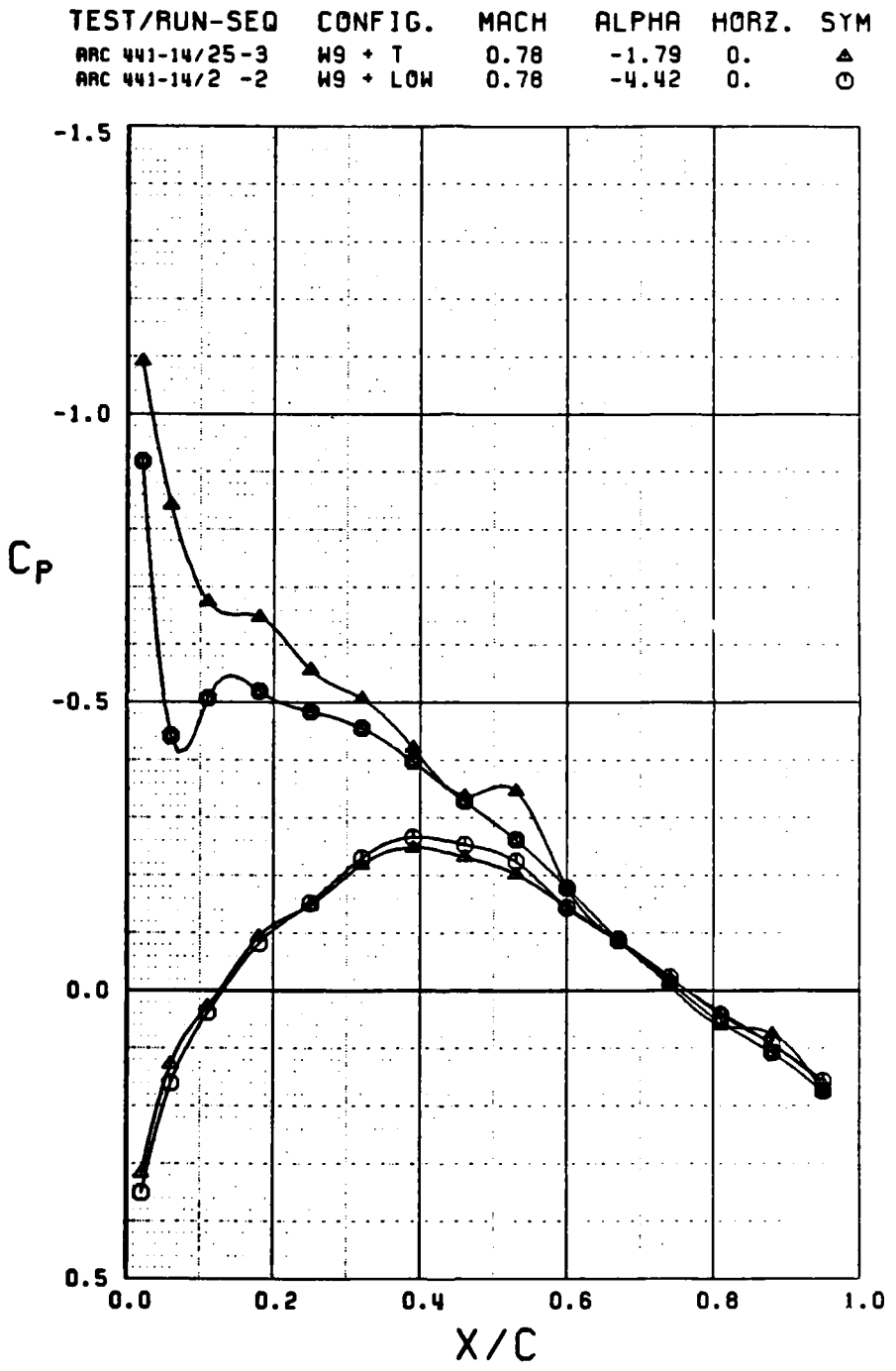

Figure 39 Low- and T-tail pressures at M_∞ =0.78, α_L =-3.4°.

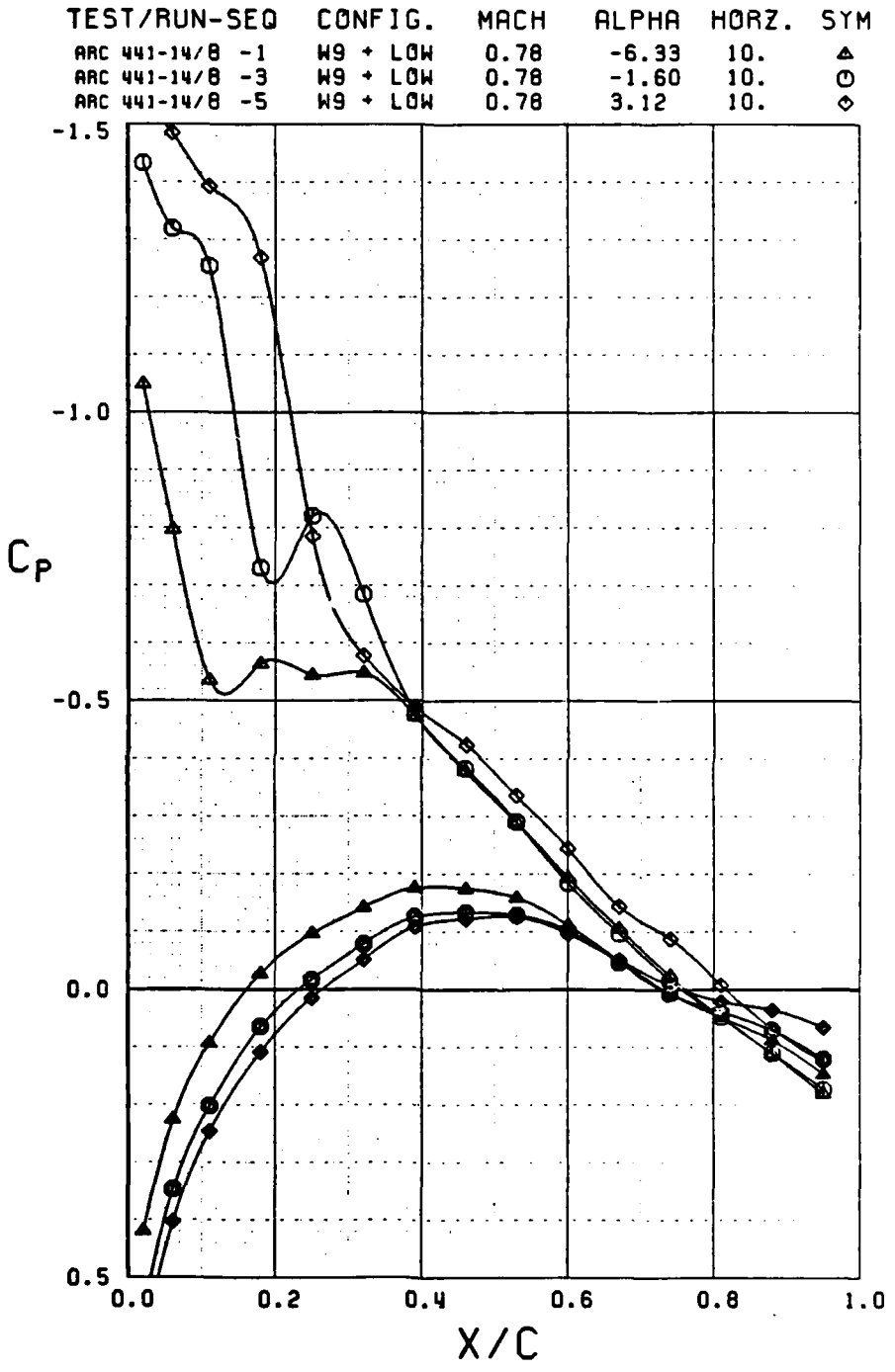

Figure 40 Angle of attack effects on the low-tail.

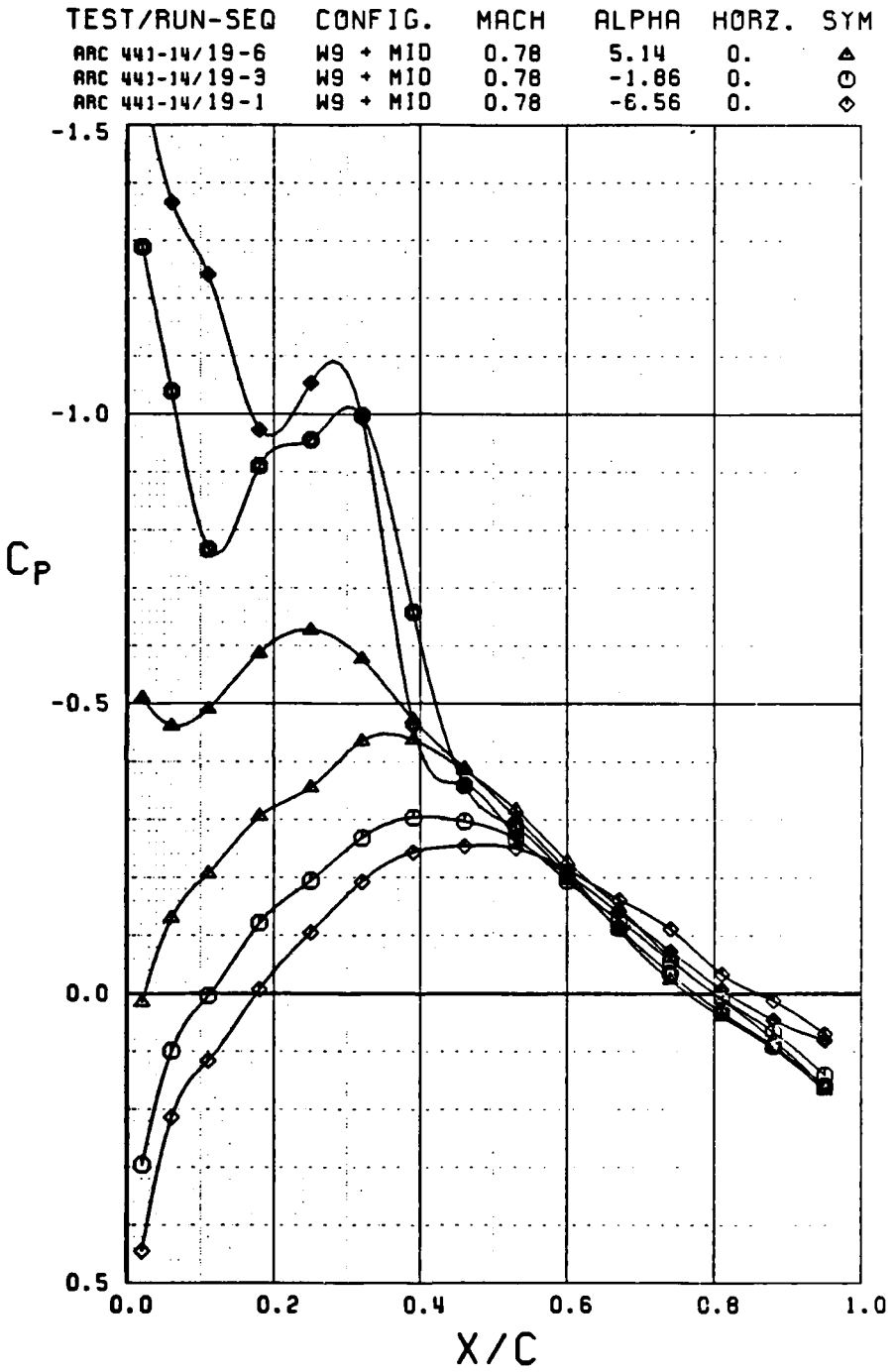

Figure 41 Angle of attack effects on the mid-tail.

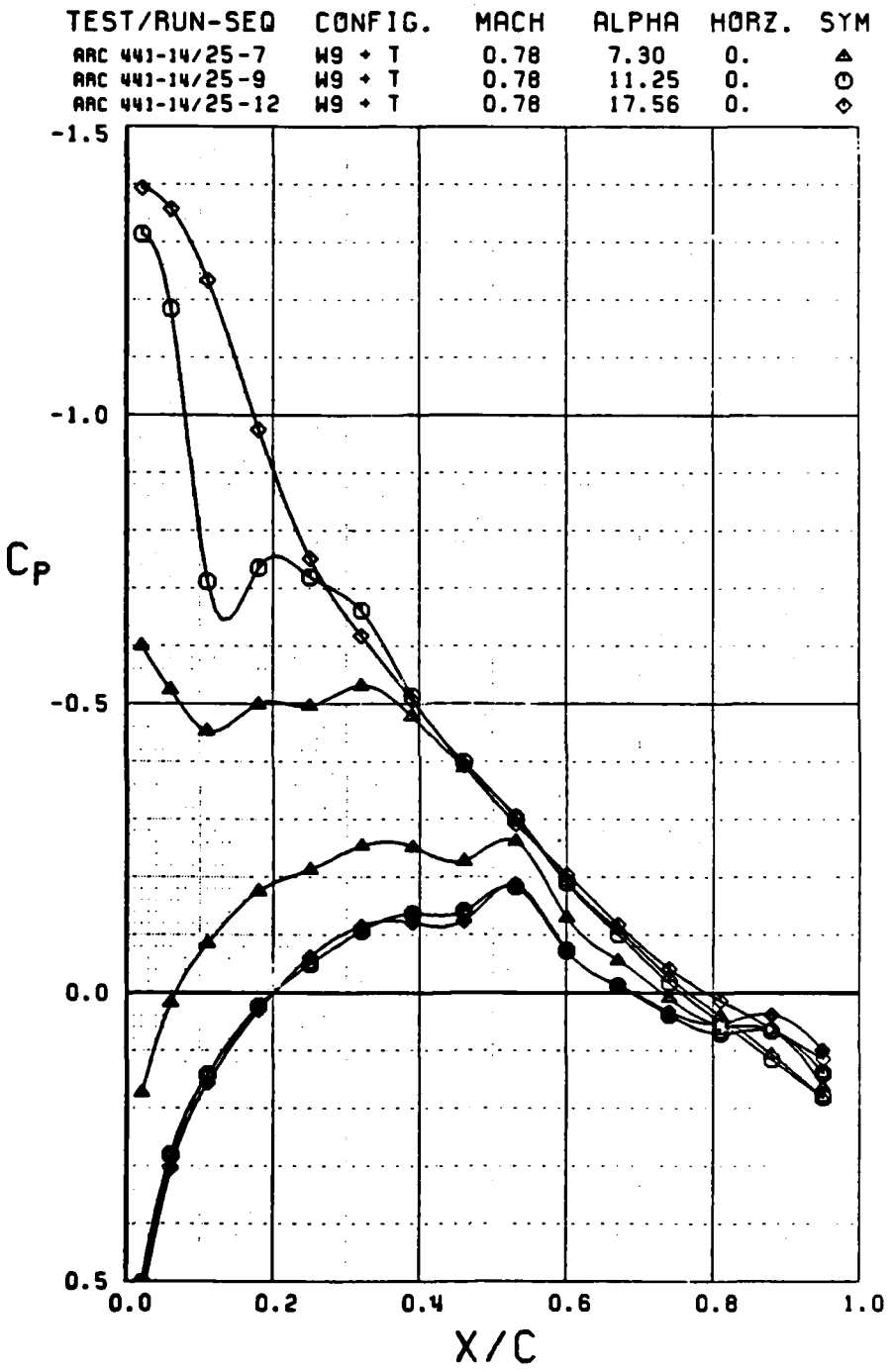

Figure 42 Angle of attack effects on the T-tail.

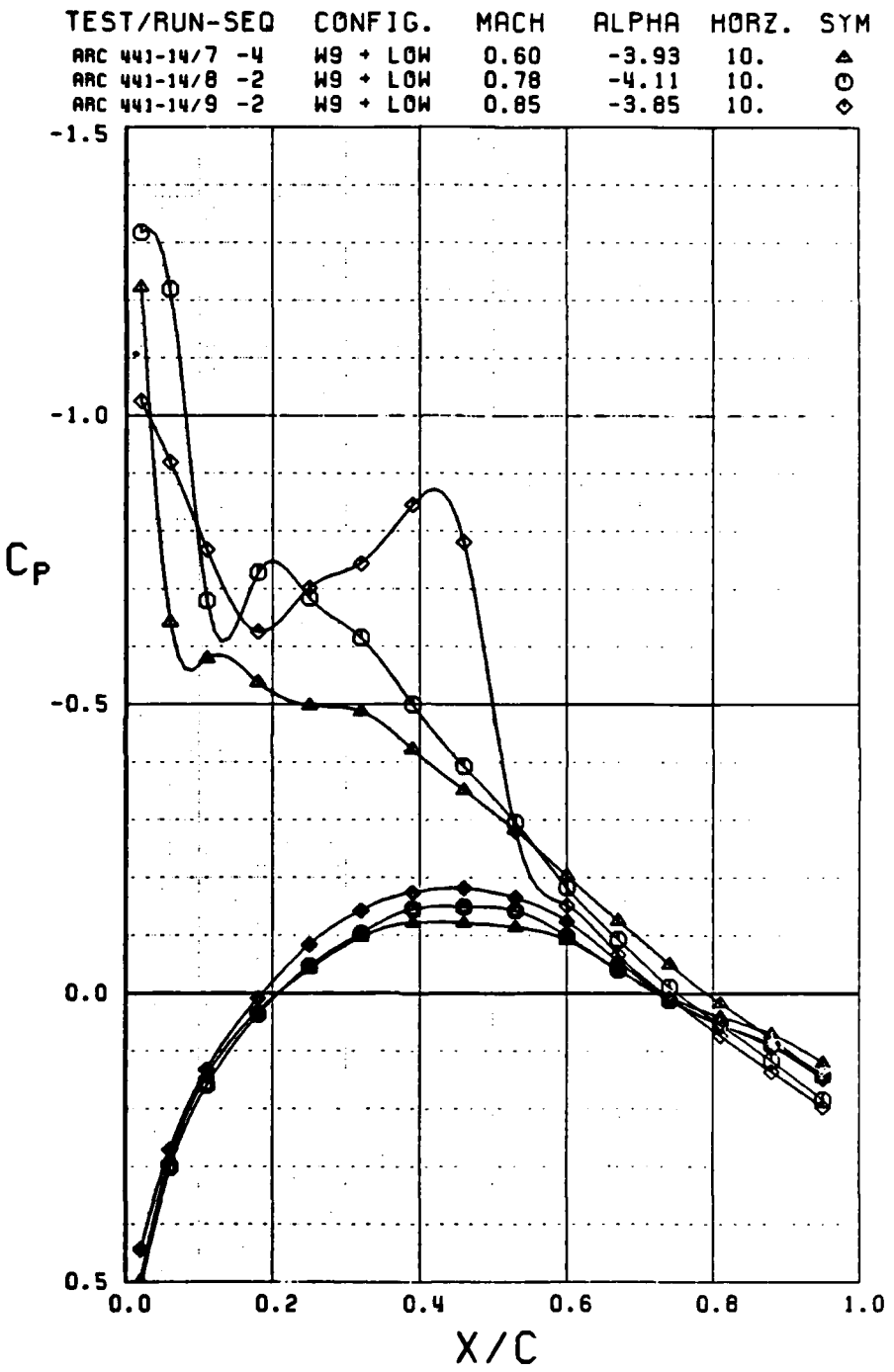

Figure 43 Mach number effects on the low-tail.

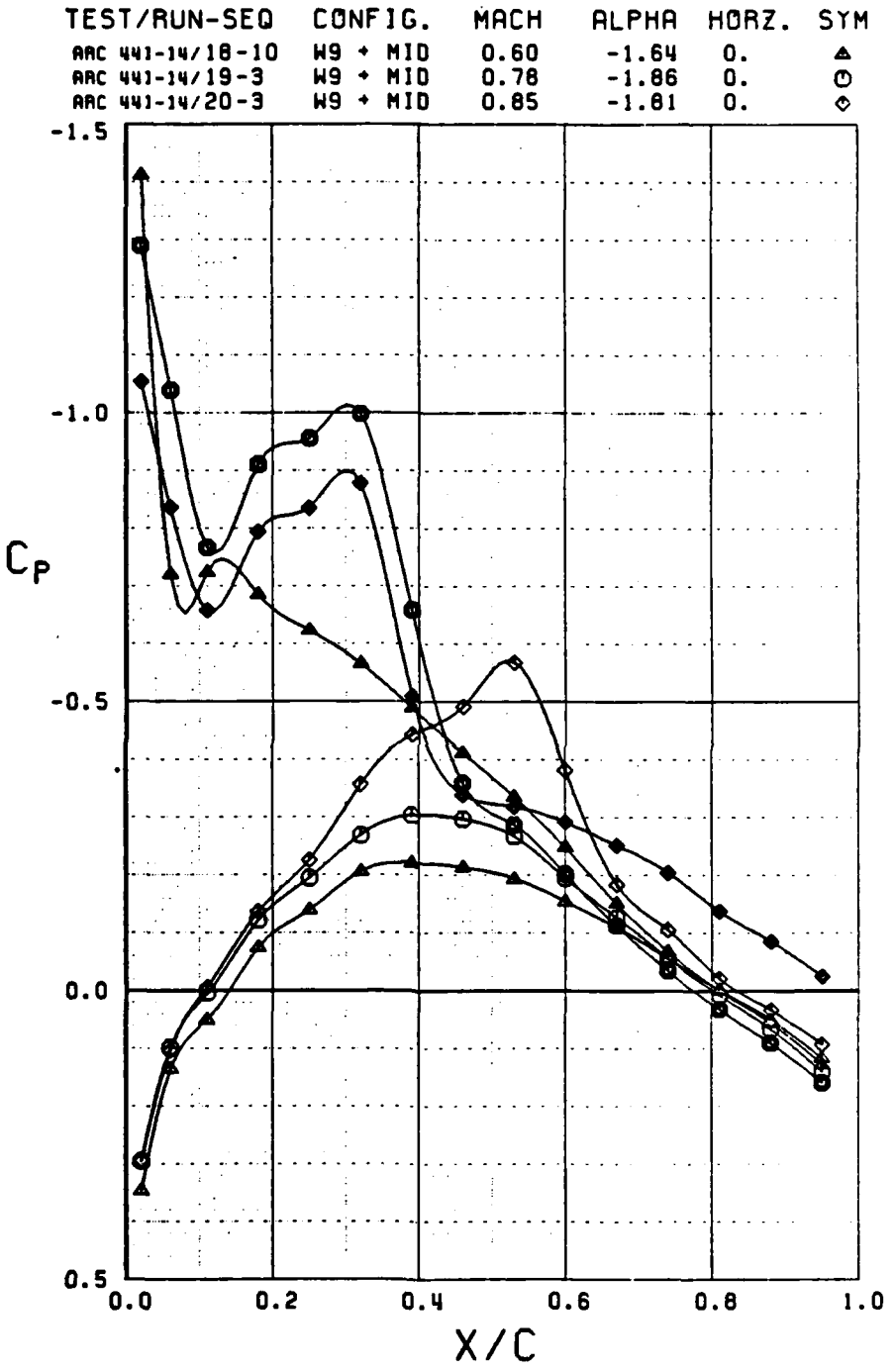

Figure 44 Mach number effects on the mid-tail.

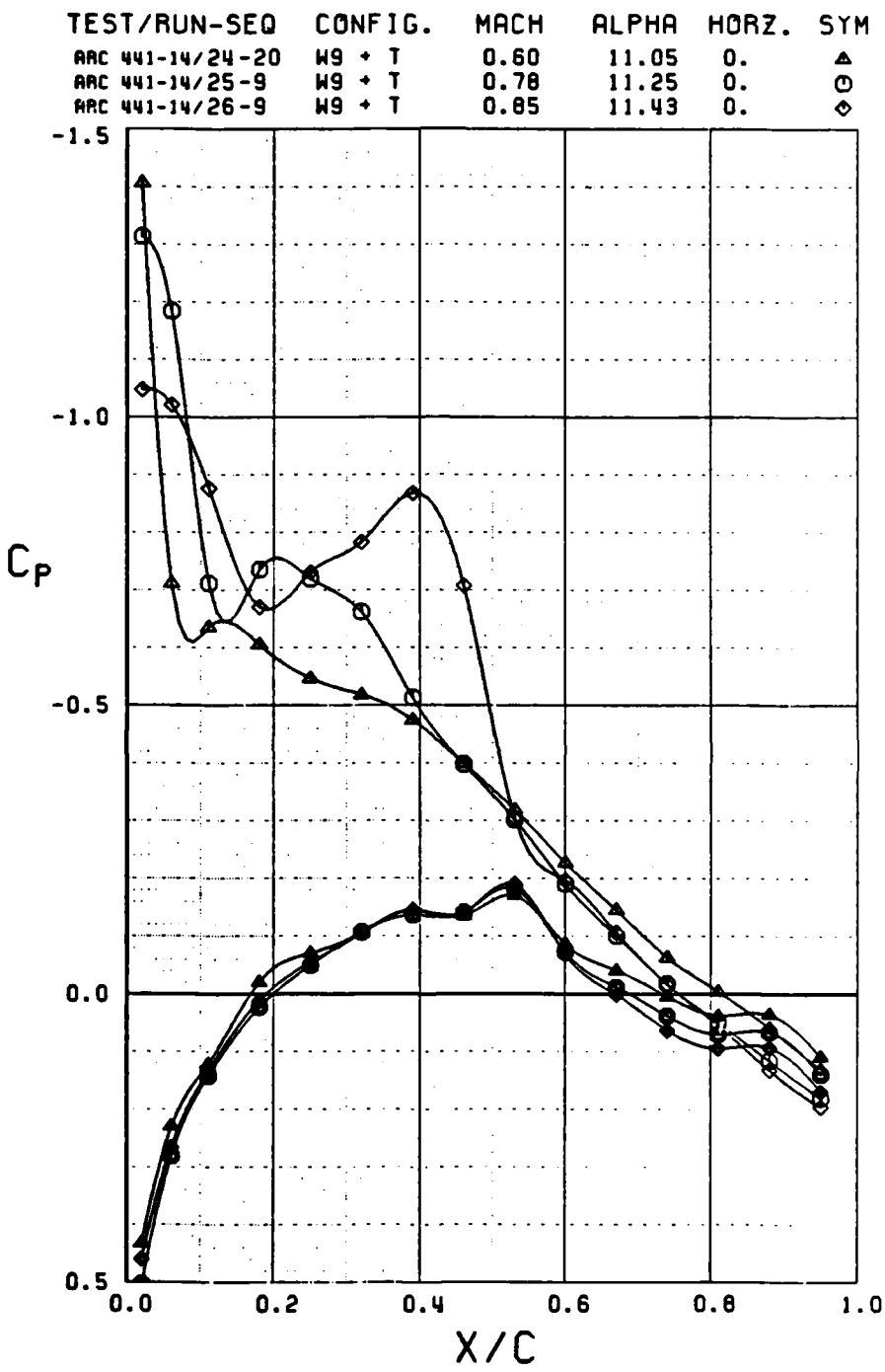

Figure 45 Mach number effects on the T-tail.

4 CONCLUSIONS

A baseline wing and a wing refined with the aid of a numerical optimization routine were tested alone and in conjunction with a low-, mid-, and T-tail. Substantial drag improvements were obtained with the refined wing; however, higher trim drag associated with a negative shift in pitching moment reduced some of the wing-alone gains.

Evaluation of the low-, mid-, and T-tails revealed flow differences between each position. However, the low- and T-tails behaved similarly when the low-tail was not adversely affected by the wing wake. An early shock formation on the mid-tail is suspected as the cause of an increase in drag associated with that tail.

REFERENCES

1. Cox, R.A., and Bhateley, I.C., "Application of Computational Methods to Transonic Wing Refinement, "Transonic Aerodynamics, edited by David Nixon, Volume 81, Progress in Astronautics and Aeronautics, American Institute of Aeronautics and Astronautics, New York, 1981.

2. Mason, W.H. and others, "An Automated Procedure for Computing the Three-Dimensional Transonic Flow Over Wing-Body Combinations, Including Viscous Effects, Vol. I - Description of Analysis Methods and Applications," AFFDL-TR-77-122, Vol. I, II, and III, 1978.

3. Holder, D.W., Pearcey, H.H., and Gadd, G.E., "The Interaction Between Shock Waves and Boundary Layers," C.P. #180, Her Majesty's Stationery Office, London, 1955.

4. Perkins, C.D. and Hage, R.E., Airplane Performance Stability and Control, John Wiley and Sons, New York, 1949.

5. Neely, R.H. and Griner, R.F., "Summary and Analysis of Horizontal-Tail Contribution to Longitudinal Stability of Swept-Wing Airplanes at Low Speeds," NASA TR R49, U.S. Government Printing Office, Washington D.C., 1959.

LIST OF ABBREVIATIONS

SYMBOLS

C_l	Rolling moment coefficient (stability axis)
C_L	Lift coefficient
C_D	Drag coefficient
C_m	Pitching moment coefficient
C_{m_δ}	Rate of change of pitching moment coefficient with horizontal tail deflection
C_n	Yawing moment coefficient (stability axis)
C_Y	Side force coefficient (stability axis)
SEQ	Run sequence number
α, ALPHA	Angle of attack (referenced to the body)
α_L	Local angle of attack
β, BETA	Angle of sideslip
ϵ	Downwash angle
ϵ_α	Rate of change of downwash with angle of attack
δ_H, DHORZ	Horizontal tail deflection angle

NOMENCLATURE

ARC	Ames Research Center
BL	Buttock line
B_{3M}	Model 603E body with two-place canopy
FS	Fuselage station
H_7	Horizontal T-Tail
H_{7a}	Horizontal mid-tail
H_{7b}	Horizontal low-tail
N_6	Flow-through engine nacelle
R_2	Vertical tail rudder

LIST OF ABBREVIATIONS (Cont'd)

NOMENCLATURE

SS	Span station
V_3	Vertical tail
WL	Waterline
W_9	Baseline steel wing
W_{10}	Modified aluminum wing

DISTRIBUTION LIST

Office of Naval Research
800 North Quincy Street
Arlington, Virginia 22217
R.E. Whitehead, Scientific Officer 1
M. Thomas, Administrative Contracting Officer 1

Director
Naval Research Laboratory
Washington, D.C. 20375
Code 2627 6

Office of Naval Research
Detachment, Chicago
536 South Clark Street
Chicago, Illinois 60605 1

Defense Technical Information Center
Bldg. 5, Cameron Station
Alexandria, Virginia 22314 12

NASA/Ames Research Center
Aerodynamics Research Branch
Moffett Field, California 94035
R. M. Hicks, M.S. 227-8 1

Naval Air Systems Command
Washington, D.C. 20361
D. G. Kirkpatrick 1